Measurements of Scalar Convection Velocity in Heated and Unheated High-Speed Jets

Sean P. Shea

Thesis submitted to the faculty of the Virginia Polytechnic Institute and State University in partial fulfillment of the requirements for the degree of

Master of Science

in

Aerospace Engineering

K. Todd Lowe, Chair

William Devenport

Wing F. Ng

Joseph A. Schetz

September 21, 2018

Blacksburg, Virginia

Keywords: Time-resolved Doppler Global Velocimetry, Scalar Convection Velocity, Unheated Supersonic Jets, Heated Supersonic Jets

Measurements of Scalar Convection Velocity in Heated

and Unheated High-Speed Jets

Sean P. Shea

ACADEMIC ABSTRACT

Jet noise has been a growing concern in recent years due to the costs associated with hearing loss of United States service members. Jet noise is also becoming more of a concern due to the rise of civilian complaints regarding the noise of jets near civilian and military air stations. One source of noise generation is from packets of air called eddies, which move with a convection velocity U_c. The current work seeks to expand upon the understanding of jet noise by collecting data using Time-resolved Doppler global velocimetry (TR-DGV) from regions of the jet known to produce high levels of acoustic radiation. Past experiments in studying convection velocity are reviewed based on the technique for obtaining the velocities. To add to these experiments, the current work analyzes data obtained using TR-DGV applied to a perfectly expanded Mach 1.65 flow with total temperature ratio (*TTR*) equal to 1. Additional measurements were obtained on a Mach 1.5 nozzle operated at a slightly over expanded condition and at *TTR* = 2. The cold jet flow is compared to the past experiments on unheated jets and demonstrates good agreement with respect to normalized convection velocities based on the jet exit speed. The data is then compared to past experiments conducted on the same nozzle at heated conditions. Shadowgraph imaging is used as a qualitative tool to locate shock cells within the jet plume. TR-DGV data from near the lipline ($r = 0.5D$) is axially aligned with the shadowgraph images to demonstrate that the shock structure within the potential core causes detectable variations in the scalar convective velocity. Additionally, it is shown that in the heated and unheated Mach 1.65 jet and the over expanded heated Mach 1.48 jet that the convection velocity does increase beyond the potential core. The Mach 1.48 jet is also compared to mean velocities obtained using Particle Image Velocimetry and found that the convective and mean velocities were only similar in some regions of the jet. A discussion is provided on suggestions of future work on where to obtain data within the jet plume and how to collect the data using current capabilities. Suggestions are also provided for improving data quality in future experiments, as well as ideas for future investigations into convection velocity along the length of the jet plume using TR-DGV.

Measurements of Scalar Convection Velocity in Heated

and Unheated High-Speed Jets

Sean P. Shea

GENERAL AUDIENCE ABSTRACT

Jet noise has been a growing concern in recent year due to the costs associated with hearing loss of United States service members. Additionally, many civilians complain about the noise of aircraft flying both out of military facilities and commercial airports. One source of noise generation is from packets of air called eddies which move with a convection velocity. Researchers have identified that by affecting the convection velocities of these eddies, there is a larger benefit than other traditional methods such as engine chevrons. The current work summarizes techniques used to investigate convective velocity as well as to provide evidence for other unconfirmed theories. This study focuses on using a laser-based technique to obtain data within the flow of an unheated supersonic jet. An unheated jet is studied to allow for easy comparison to other experiments that have used different diagnostic techniques. Additionally, this case is studied to complete a set of experiments that were previously conducted on the same nozzle so that there is a true base-line or "control" case for future work. Later in this paper, analysis will be done to show how shocks within the jet affect the convective velocity. A combination of both quantitative and qualitative efforts are performed to accomplish this. Additionally, it will be shown that after the potential core of the jet breaks down, there is an increase in the local convective velocity in this region immediately after the potential core. Finally, a brief summary will be given and suggestions for future work will be presented.

Acknowledgements

A special thanks to Dr. Lowe and Dr. Ng. Words cannot express how grateful I am to have worked with you over the past three years. Through the highs and lows, your guidance has helped me to grow so much and I will be forever thankful to have worked under you both.

Thanks to the Office of Naval Research and Dr. Knox Millsaps. This work is sponsored by Navy grants N00014-16-1-2444 and N00014-14-1-2836. Additionally, thanks to NASA and NAVAIR, including John Sparopulous, for funding other parts of my time during graduate school.

Thank you to all of my friends in graduate school that I have met over the years. You all have been such a huge support through the struggles of graduate school and I wish you all the best of luck in academia and in your careers to come. A special thanks to Nick Albertson, Agastya Balantrapu, Matthew Boyda, Dan Cadel, Kara Crosser, Kyle Daniel, Aaron Defreitas, Will George, Tamy Guimarães, David Mayo, Anthony Millican, Nick Molinaro, Eric Rolfe, Matthew Ruda, Ashley Saltzman, Kevin Silas, Dillon Sluss, Marcie Stuber, Tyler Vincent, and Chi Young Moon.

Thanks to everyone at NLCF, my family away from home, especially Christian Hurl and Robbie Poff. The two of you have been so much help over the past two years and I cannot thank you enough.

Finally, I would like to thank my family for all that they have done for me over my life. I could not have gotten to this point without you.

Table of Contents

Nomenclature

a_0	Ambient speed of sound
D	Nozzle exit diameter
f	Frequency
f_j	Optical deflectometer signal
g	Delay-and-sum output from beam-formed microphone
H	Fourier transform of h
h	Delay-and-sum output from optical deflectometer
k	Wave number
M	Magnification multiplier [pixels/m]
M_c	Eddy convective Mach number
M_d	Design Mach number
M_j	Jet Mach number
m	Mode number
N	Generic for a number of samples
P	Equivalent signal from passive scalar
p	Pressure
Re	Reynolds number
r	Radial coordinate from jet centerline
S	Fourier transform of auto spectrum
St	Strouhal number. $St = f D/U_j$
S_b	Baseline signal
S_s	Signal from collected light
s	General zero-mean signal variable
T	Data collection time period
T_{OD}	Optical deflectometer time delay
T_{ij}	Lighthill stress tensor
TTR	Total temperature ratio
t	Time
U_c	Convection velocity

U_j	Jet exit velocity
u	Velocity fluctuation
x	Axial coordinate from nozzle exit
Δp	Pixel spacing on sensor
Δx	Distance between sensors in flow
$\Delta \tau$	Peak correlation lag time
δ_{ij}	Kronecker delta
ω	Angular frequency
ϕ	Mach wave angle
ρ	Density
ρ_0	Ambient air density
σ_{ij}	Viscosity tensor
τ_m	Microphone time delay
θ	Polar angle relative to jet axis
ξ, ς	Spatial coordinate

1. Introduction

In recent years, members within United States Navy have become increasingly concerned with sources of hearing-related disabilities of both current and retired members of the armed forces. According to a report published in 2017 by the Department of Veterans Affairs, the most prominent service-related disabilities receiving compensation were hearing loss and tinnitus [1], a disability characterized as a ringing sound within the ear with no outside source of sound, caused by prolonged exposure to high decibel noise sources [2]. Of the almost 21.4 million reported disabilities, 12.6% of these cases consisted of hearing loss or tinnitus; when looking at the most prominent cases of service-related disabilities, the prevalence of hearing loss and tinnitus jumps to 34.2% [1]. Some advance hearing protection has been developed by the Navy to help reduce noise levels experienced by crewmen by 47 dB; however, this method of protection is very expensive and is not universally used throughout the entire fleet [3]. Even with this significant reduction in noise exposure, there is still a gap between the sound level experienced by crewmen (approximately 100 dB) and what is considered safe by the Occupational Health and Safety Administration (OSHA), 85 dB [4]. In order to close this gap, more research needs to be done on how jet noise is produced and how engine nozzles can be modified to reduce the noise level, while still meeting the requirements necessary for military aircraft to complete their missions.

As Naval aircraft are required to adapt to a changing combat environment to become more agile, to have increased range, and to operate at faster speeds, there comes a cost in that the engines that provide the power to meet these needs also produce more noise. Not only does this impact missions that require stealth, but also the crewmen aboard naval carriers and people in close proximity to naval bases. Some techniques have been implemented such as adding chevrons or fluidically enhanced chevrons to the exits of afterburning engines, but these systems add weight to the aircraft and often require large amounts of maintenance and funding to maintain effectiveness [3]. This leaves open the opportunity for researchers to study other mitigation methods and study locations of peak noise generation to target for noise reduction.

Sources of jet noise have been studied for many years with one source identified as being the development of turbulent eddies within developing shear layers of supersonic flows. In these regions, the convective Mach number M_c is indicative of the efficiency of the radiated sound [5]. As noted by Papamoschou et al. [5], a non-linear scaling exists between the radiation efficiency of eddies and the convective Mach number. Further study of this relationship and locations of high convective Mach number within a jet plume will allow researchers to target regions that will offer the most potential for noise reduction.

To further the understanding of how convection velocity varies within jet plumes, time-resolved Doppler Global Velocimetry (TR-DGV) was applied to a Mach 1.65 flow with a total temperature ratio (*TTR*) of 1, and is commonly referred to as an "unheated" or "cold" jet due to the fact that heat was not added to the flow. This unheated jet uses the same biconic nozzle geometry studied by Ecker et al. [6,7,8,9] with the goal of expanding upon their findings through obtaining a dataset with a higher resolution of data points and comparing the current data set with the heated (*TTR* = 1.6 and *TTR* = 2.0) data sets obtained by Ecker et al. [7,8]. Additionally, data was taken on a contoured nozzle with design Mach number 1.5 operated with a *TTR* = 1.83 and slightly over expanded at Mach 1.48. This nozzle has been studied by Mayo et al. [10,11] and was found to originally found to produce weak shocks within the plume. While the unheated data set will be used to compare with those of other researchers, both heated and unheated data sets will be used to highlight some observations in the current work that the convection velocity within the core region of the jet is affected by the shock structure within the flow and to show an increased convection velocity beyond the breakdown of the potential core. The potential core is defined as a region of near constant mean velocity and extends from the nozzle exit to the axial station where the centerline velocity is 95% of the exit velocity. Finally, mean velocities obtained using Particle Image Velocimetry will be compared with convection velocities obtained using TR-DGV under similar conditions to test a hypothesis by Bridges and Wernet [31] that convection velocity can be approximated as mean velocity, especially within the developing shear layer that exists between a jet of air and the ambient medium which is known to contribute to jet noise.

1.1 Overview

This thesis is broken down into six chapters and three appendices with supporting work related to hardware capabilities and data analysis techniques. Chapter 1 gives an overview of why the topic of jet noise is relevant to the Navy and briefly discussing the overall topic of this thesis. The second chapter provides a review of literature pertaining to past work on unheated jets by other research groups and the past work on the current nozzle geometry for heated conditions. This will include a brief overview of the TR-DGV system used in previous experiments on heated jets using the same nozzle geometry. Chapter 3 will focus on the experimental methods pertaining to the current experiment using the *TTR* = 1, Mach 1.65, and *TTR* = 1.83, Mach 1.48 data. The fourth chapter will focus on the result of the current work as well as a comparison to the convection results with those of the heated jet studied by Ecker et al. [7,8], as well as provide discussion on comparisons to other experiments on heated and unheated jets. Section 5 will offer a discussion on future work pertaining to both experimental locations for further study of convection velocity in a jet, as well as, improvements for obtaining better quality data. The final chapter will summarize the conclusions for the current work.

2. Review of Relevant Literature

The following section is broken up into two different sections. The first section, Section 2.1 gives a brief overview of the fundamentals of jet noise and the importance of looking at convection velocity. Section 2.2 will discuss past techniques used to measure convection velocity derived from pressure fluctuations and also convection velocity of passive scalars which is the convection velocity of a seeding particulate introduced into a flow. A final use of this section will be to act as a catalog of data from these works for ease of use for future work. Finally, Section 2.3 will discuss the motivation for the current work based on these past studies.

2.1 Fundamentals of Jet Noise

The investigation of how sound was produced by a fluctuating flow was first studied in-depth by Lighthill [12] in 1952 in which he sought to relate flow properties to acoustic properties.

Through his studies, Lighthill was able to relate the Navier-Stokes equations, which govern physics of a flow, to the wave equation, which govern acoustic properties within a fluid flow. After relating the Navier-Stokes and wave equations, Lighthill re-cast the equation and noted that several terms were not a part of the linear propagation of the wave equation resulting in Lighthill's Equation shown in Equation (2.1). The left side of Equation (2.1) is the wave equation, while the right side was identified as being the sources of noise within the jet.

$$\frac{\partial^2 \rho}{\partial t^2} - a_0^2 \nabla^2 \rho = \frac{\partial^2 T_{ij}}{\partial x_i \partial x_j} \tag{2.1}$$

$$T_{ij} = \rho u_i u_j + (p - a_0^2 \rho)\delta_{ij} - \sigma_{ij} \tag{2.2}$$

From Equation (2.2) we see that the sources of noise in can be attributed to Reynolds stresses, pressure, viscous forces, and stresses within the flow. Since the flow rests in a uniform stagnent atmosphere, the stress tensor coulld be further simplified by neglecting stresses outside of the flow. Furthermore, Lighthill stated how the viscous stresses are very small and can be assumed as zero, as well as noting that the temperature difference in low Mach number flow with its surroundings is only due to kinetic effects, such as frictional heating or cooling by expansion. This yielded the approximate form of the Lighthill stress tensor as Equation (2.3).

$$T_{ij} \approx \rho_0 u_i u_j \tag{2.3}$$

In order to develop this stress tensor, Lighthill limited his analysis to that of a subsonic flow [12]. Since jet noise problems are concerned with high speed flows, several researchers worked to improve upon the analogy, starting with Ffowcs-Williams in the 1960s [13]. Ffowcs-Williams improved upon the analogy by considering convection on the acoustic intensity by multiplying the intensity by the factor shown in Equation (2.4) and is known as the convection amplification factor.

$$|1 - M_c \cos\theta|^{-5} \tag{2.4}$$

$$M_c = \frac{U_c}{a_0} \tag{2.5}$$

The factor takes into account the convective Mach number M_c, shown in Equation (2.5) and an angle θ relative to the jet axis. Further improvements have been made to the analogy by Ffowcs-Williams and Maidanik [14], Goldstein and Howe [15], and Ribner [16].

More recently, in 2014, Papamoschou et al. [5] furthered the acoustic analogy showing that noise radiation efficiency is influenced and scales linearly with turbulence intensity within the flow. Additionally, Papamoschou et al. found that the radiation efficiency is also influenced by the convective Mach number with a non-linear relation. The authors go on to state that focusing on a reduction in convective Mach number is a more effective target for reducing jet noise, as a 50% reduction in turbulence intensity only equates to a 3 dB reduction in the observed noise level, while a one-third reduction of convective Mach number equates to a reduction in observable noise by 10 to 15 dB. This finding exemplifies the importance of understanding and measuring the convective velocity of turbulent eddies within a jet plume.

2.2 Past Investigations into Convection Velocity

Over the past twenty-plus years, investigations into the convection velocity of turbulent eddies within developing shear layers have been conducted using a myriad of different experimental techniques. These techniques range from simple microphone and shadowgraph setups to more complex time-resolved particle image velocimetry (TR-PIV) and time-resolved Doppler global velocimetry setups. Section 2.2.1 reviews obtaining convection velocity from Shadowgraph imaging. Section 2.2.2 will discuss several experiments that used optical deflectometry to obtain convection velocity. Section 2.2.3 focuses on the use of phase evolution of wavepackets. Section 2.2.4 will look at computations using Proper Orthogonal Decomposition (POD) of Computational Fluid Dynamics (CFD). Sections 2.2.5 and 2.2.6 will focus on experiments using TR-PIV and TR-DGV, respectively, to measure convection velocity. Especially of note, the measurements reviewed in section 2.2.6 will consist of measurements that were obtained on the same Mach 1.65 nozzle discussed in the current work.

2.2.1 Convection Velocity from Shadowgraph Images

Some methods for studying convections velocity are less complex than other laser-based techniques, which will be discussed in later sections. One of these simpler methods utilizes

shadowgraph imaging to obtain images of a flow field. Typically, shadowgraph imaging is used to qualitatively study shocks and expansions within a flow-field due to its sensitivity to the second derivative of density. The system depicted in Figure 2.1 utilizes a point light source directed at a parabolic mirror. The light is then directed at two planar mirrors to align the light in perpendicular rays. The light is then sent toward a final parabolic mirror and into a camera located at the focal point of the parabolic mirror.

Some advantages of a shadowgraph system include being non-intrusive and that the technique does not depend upon adding seeding to the flow. This ensures that the measurement techniques do not interfere with the flow or change its properties. A disadvantage of this technique is that the photos require some post-processing as they do not directly measure convection velocity.

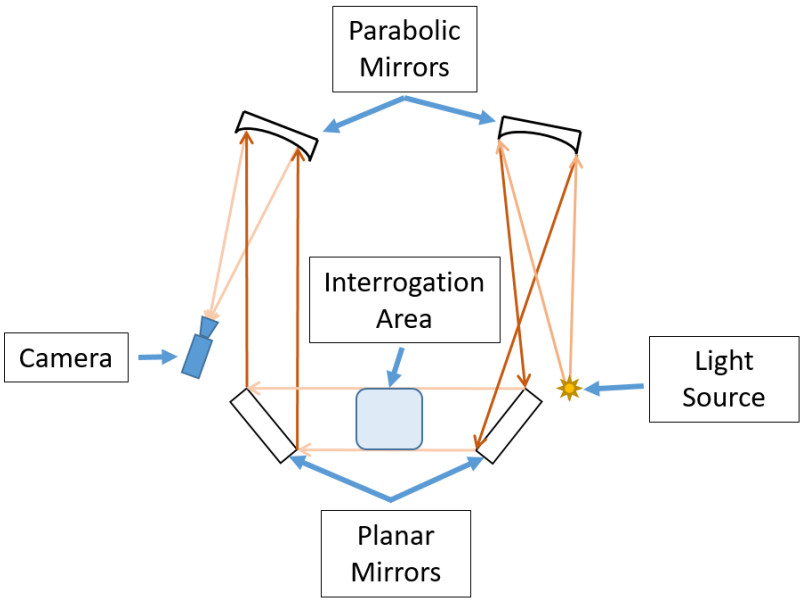

Figure 2.1 Example Shadowgraph system

In 2016, Murray and Lyons [17] demonstrated that it is possible to extract quantitative data from shadowgraph images by using a Radon transformation to measure the Mach wave angle Φ of the shock fronts which emanate from the jet and using Equation (2.6).

$$\Phi = \arccos\left(\frac{1}{M_c}\right) \tag{2.6}$$

An example of these shock fronts can be seen in Figure 2.2 which is extracted from Murray and Lyons [17], with permission, to point out the shock fronts in the shadowgraph images which appear as lighter grey striations on the edge of the jet plume and within the ambient medium. It should be noted that these are also the same shock fronts that are attributed to the crackle noise phenomenon in some supersonic jets.

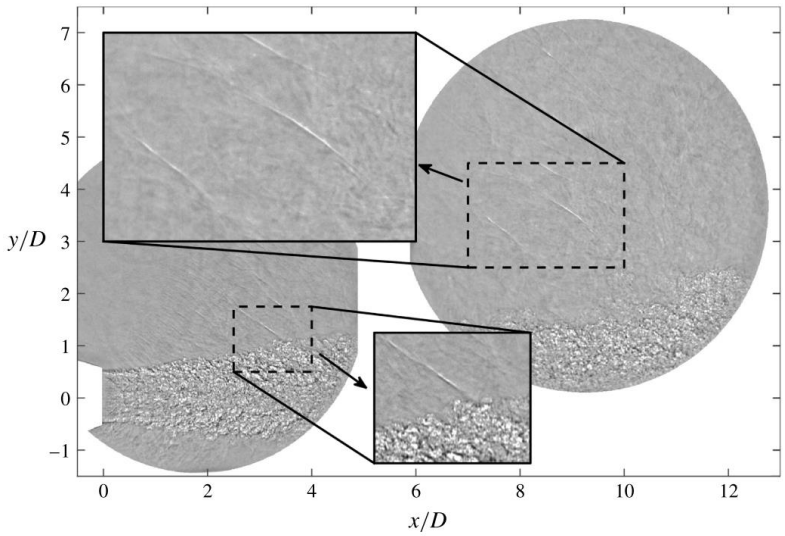

Figure 2.2 Example of shock fronts taken with permission from Murray and Lyons [17].

In their work, Murray and Lyons discuss how the location of the convective velocity of coherent density fields is backed out of the shadowgraph images. The authors state that these shock fronts emanate from a location within the shear layer perpendicular to their surface. The authors also noted that at any given point in the shear layer, there were multiple different convection velocities present with certain velocities being more dominant and coincide with the standing shock waves within the potential core.

Murray and Lyons looked at two different nozzle geometries operated at Mach 1.55; one is a more standard converging-diverging shape, while the other is a converging-diverging nozzle with contoured inserts designed to help reduce jet noise. It should be noted that the standard converging-diverging nozzle was designed to operate at Mach 1.74 and thus was operated at an over-expanded condition while the other nozzle was operated at is design condition. These jets were operated under heated conditions and the measured average convection velocities ranged from approximately $0.63U_j$ to $0.75U_j$ for the standard geometry and $0.54U_j$ to $0.79U_j$ for the

geometry with contoured inserts. Figures 2.3a and 2.3b display the mean convection velocities obtained by Murray and Lyons for the baseline and contoured nozzles, respectively.

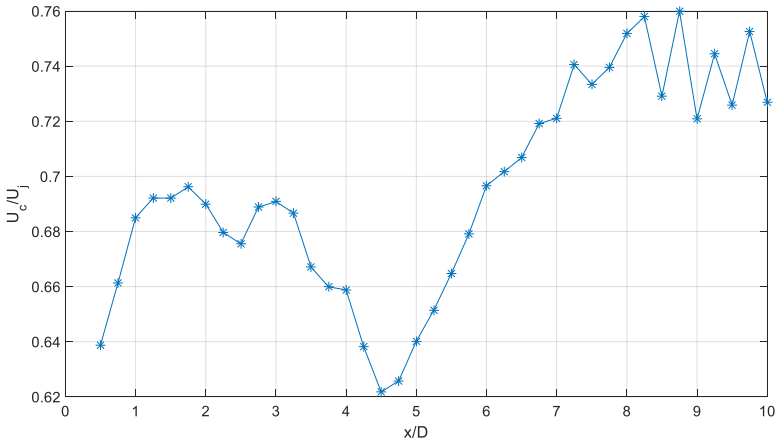

Figure 2.3a Mean convection velocity within the shear layer for a round nozzle [17].

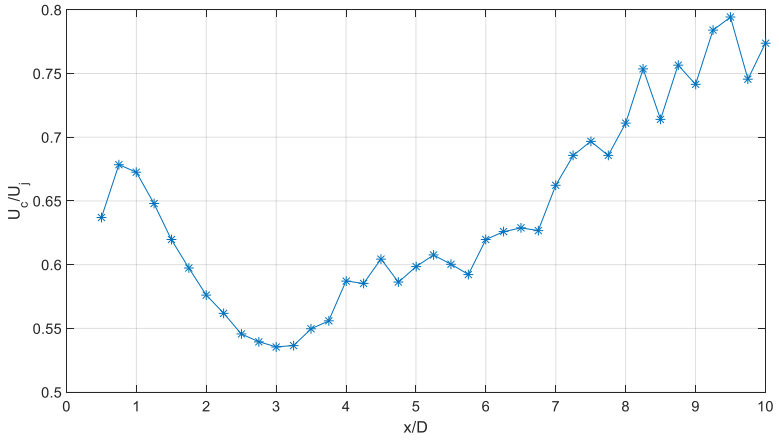

Figure 2.3b Mean convection velocity within the shear layer for the round nozzle with contoured inserts [17].

2.2.2 Convection Velocity from Optical Deflectometry

Optical Deflectometry (OD) is another method that can be used to measure convection velocity within a fluid flow and was first described by McIntyre and Settles [18] and McIntyre [19]. This technique was further improved by Alvi et al. [20] and Garg and Settles [21] in the 1990s to use the Schlieren imaging technique. This technique uses a point light source directed at a parabolic mirror and then into a fluid flow. Light passes through the flow and is then directed by another

parabolic mirror toward imaging hardware. At the focal point of the mirror, a knife edge is placed to partially block the light which then expands and passes through a 50/50 beam-splitter and on to two photomultiplier tube sensors (PMTs). These sensors have most of their detective faces blocked except for a small pin-hole aperture which acts as a probe within the collected image. Since this technique is set up as if it were a Schlieren system, the PMTs are measuring changes in the refractive index of light and is sensitive to the first derivative of density. One PMT remains stationary, while another is moved horizontally to capture data throughout a measurement window. Unlike a Schlieren system where the data collected is spatially resolved [22], the use of PMTs allows for the data to be time-resolved and to easily perform two-point correlations to compute the convection velocity.

More recently, several groups have used optical deflectometry to study convection velocities of coherent density fields within the plume of a jet. Doty and McLaughlin [22] used OD to measure the convection speed in both pure air and helium/air jets at Mach 0.9 and Mach 1.5 emanating from a round nozzle. A mixed gas jet was used to simulate a heated jet condition in the Pennsylvania State University high-speed jet noise facility. One limitation noted by the authors of this study was that the data acquisition technique is not capable of obtaining measurements within the inner regions and core of the jet. Due to the technique being very similar to Schlieren imaging, the effective focus depth within the flow is 5 mm before the sensitivity is reduced.

Doty and McLaughlin found that for the Mach 0.9 pure air jet was approximately $0.75U_j$ along the lipline and $0.78U_j$ for the Mach 1.45 flow (the jet was operated below Mach 1.5 in order to stay on condition). Both of these values are presented for the lipline location at $4D$ from the nozzle exit although data was taken between $4D$ and $6D$ in increments of $0.25D$ (one PMT sensor remains stationary at $4D$ while the other is moved in the $0.25D$ increments). For the simulated heated cases, the convection velocity was $0.49U_j$ for the Mach 0.9 case and $0.46U_j$ for the Mach 1.47 case. It was noted that there was an increase in the uncertainty of the convection velocities in the heated cases due to correlations being less correlated. The authors believe this to be due to the fact that smaller scale structures dominate the density gradients and essentially hide the larger scale turbulence.

Similarly, Petitjean et al. [23] also looked at different geometric nozzle shapes using OD. Three geometries were tested, a round nozzle and two beveled nozzles with varying bevel lengths. However, for the purposes of the current work, only the round nozzle geometry will be discussed further. Data for this experiment was taken in the Low Speed Aeroacoustics Facility at Boeing at three different speed conditions: Mach 0.6, Mach 0.9, and Mach 1.5. Additionally, all of the conditions were conducted on unheated flows. The data was taken between 4*D* and 5.5*D* downstream of the nozzle exit along the shear layer in increments between 0.1*D* and 0.25*D*. For this set of experiments, the convection velocity at 4*D* was found to be $0.71U_j$ for the Mach 0.6 case and $0.74U_j$ for the Mach 0.9 and 1.5 cases.

2.2.2.1 Convection Velocity Using Optical Deflectometry Correlated with Beam-formed Microphone Arrays

Papamoschou et al. [24] further improved upon the OD technique with the addition of far-field pressure measurements using a beam-formed microphone phase array and using a delay-and-sum (DAS) signal for both techniques. This DAS signal is the summation of signals $p_m(t)$ from a microphone m and the acoustics propagation time $\tau(\xi)$ from a point ξ. This DAS relationship can be seen in Equation (2.7).

$$g(\xi, t) = \sum_{m=1}^{M} p_m(t + \tau_m(\xi)) \tag{2.7}$$

The equation of the DAS signal for the OD uses the summation of the OD signals $f_j(x,t)$ and can be seen in Equation (2.8), with the optical deflectometry time delay term $T_{OD,j}$ defined in Equation (2.9). It should be noted that the OD used in this experiment was developed by Veltin et al. [25] to use four PMT sensor instead of the usual two.

$$h(x, t) = \sum_{j=1}^{J} f_j(x, t + T_{OD,j}) \tag{2.8}$$

$$T_{OD,j} = \frac{\Delta x_j}{U_c} \tag{2.9}$$

In this work, the authors demonstrated that by maximizing the variance of the DAS signal of the OD, it is possible to determine the convective velocity within the flow. The variance can be seen in Equation (2.10) where $S_{hh}(x,\omega)$ is the Fourier transformation of the auto-spectrum of the DAS signal of the OD in Equation (2.8) and is presented in Equation (2.11) Note in Equation (2.11) that * represents a complex conjugate of a Fourier transform.

$$\sigma_h^2(x) = \int_0^\infty S_{hh}(x,\omega)d\omega \tag{2.10}$$

$$S_{hh}(x,\omega) = \langle H(x,\omega)H^*(x,\omega)\rangle \tag{2.11}$$

This work by Papcmoschou et al. was on an unheated jet operated at Mach 1.75 as several axial stations. Table 2.1 summarizes the convection velocities presented in this paper along with their location in the flow. It should be noted that most of the data is presented near the lipline except for the final case where it is presented at the jet centerline. Additionally, the axial location reported is that of the reperence probe for the OD.

Table 2.1 Summary of Convection Velocities

Axial Location ***x/D***	**Radial Location** ***r/D***	**Convection Velocity** U_c/U_j
2.0	0.48	0.83
3.5		0.81
10		0.83
10	0	0.89

In this work, the authors also commented on this technique of using beam-formed OD signals (having multiple OD probes) as opposed to only a single probe with the microphone array. Researchers found that the beam-formed OD offered better fidelity and higher coherence levels of isocontours than with the single probe which will allow for better research for predictive noise models in the future. Additionally, the researchers found that the peak noise radiation related to the convective velocity is coherent over a large axial distance, leading to evidence to support the research of large-scale structures in high-speed jets and studying their effect upon jet noise.

2.2.3 Convection Velocity from Pressure Fluctuations

This section is split into two sub-sections both concerned with obtaining convection velocity from pressure fluctuations. Section 2.2.3.1 will discuss the use of Proper Orthogonal Decomposition (POD) of Computational Fluid Dynamics (CFD) simulations. Section 2.2.3.2 will touch on a study that was experimentally based and used dominant modes from microphone measurements. Although the authors did not compute convection velocity, the results provided in the paper were used to extracted convection velocity of wavepackets having various frequencies along the length of the flow.

2.2.3.1 POD from Pressure Fluctuations in CFD

Proper Orthogonal Decomposition has been applied to compute and estimate convection velocity using Unsteady Reynolds-Averaged Navier-Stokes (URANS) equations for a military-style nozzle with an unheated bypass and heated core [26]. In this simulated experiment, Du and Morris first calculated the overall convection velocity for three computational cases for a Mach 1.5 flow. The first CFD simulation consisted of a single standard heated jet. Test Case 2 consisted of a heated core with unheated bypass at with a core total temperature TTR_{core} = 3.0. The final case had a TTR_{core} = 3.6 with an unheated bypass. These three cases are summarized in Table 2.2.

Table 2.2 Summary of Test Cases Abbreviated from Du and Morris [26]

Test Case	TTR_{core}	TTR_{bypass}	TTR_{mixed}
1	3.0	-	3.0
2	3.0	1.0	2.6
3	3.6	1.0	3.0

The data to compute the convection velocity was collected along the lipline using virtual probes and two-point space-time cross-correlation between $x = 2D$ and $x = 6D$ from the simulated nozzle exit. Convection velocity ranged from $0.45U_j$ to $0.56U_j$; however, the convection velocity was comparable for all cases along the lipline.

Additionally, convection velocity was computed through the use of Proper Orthogonal Decomposition (POD), a technique used to find dominant modes at specific frequencies. For this study, researchers focused on Strouhal numbers of 0.3 and 0.6 as these were identified as have the largest noise radiation levels over several different polar angles. After applying POD to the

pressure data, mode 0 was identified as the dominant mode. To compute the convection velocity for this dominant mode Equation (2.12) may be used.

$$U_c = \left|\frac{\omega}{k}\right| \tag{2.12}$$

In the above equation, ω is the angular frequency of pressure fluctuations within the flow and k is the wavenumber inferred from the slope of the phase curve of the dominant POD mode.

The authors noted that noise sources corresponding to a Strouhal number of 0.6 peaked in intensity near the nozzle exit and fell off further upstream. These high-frequency noise sources moved with an average convection velocity of $0.68U_j$ between the three test cases. The noise sources at Strouhal 0.3 were noted as acting throughout the jet stream and had an average convection velocity of $0.64U_j$ between the various test cases.

2.2.3.2 Convection Velocities from Dominant Modes in Microphone Measurements

Sinha et al. [43] conducted several experiments which looked at how fluidic injections changed the noise output from a supersonic jet operated at Mach 1.5 and under heated conditions where *TTR* = 1.74. These experiments, conducted at the United Technologies Research Center in the Acoustic Research Tunnel, utilized a rotating microphone array to collect nearfield acoustic measurements. From these measurements, researchers were able to compute modal phases for the first two modes ($m = 0$ and $m = 1$) of the near-field measurements along the entire measured jet axis between approximately $x = 3D$ and $x = 15D$ for $St = 0.1$, 0.2, 0.25, 0.4, and 0.5. From the slope of the phase curves, which are plotted with phase on the y-axis with the units of radians and *x/D* on the x-axis, the wavenumbers were computed. Angular frequencies were computed knowing *St* and estimating the jet exit velocity to be 564 m/s at an estimated atmospheric temperature of 293 K. Convection velocities were then computed using Equation (2.12). Table 2.3 summarizes the calculated convection velocities. Note that the slope reported has been non-dimensionalized by the reported nozzle diameter of 0.0508 m.

Table 2.3 Convection Velocities Estimated from [43]

St	f [Hz]	m	Slope from Phase Curve	k [m^{-1}]	U_c/U_j
0.1	1110	0	1.24	24.4	0.51
		1	1.33	26.2	0.47
0.2	2220	0	1.94	38.2	0.65
		1	2.19	43.1	0.57
0.25	2780	0	2.30	45.3	0.68
		1	2.77	54.6	0.57
0.4	4440	0	3.54	69.7	0.71
		1	4.16	81.8	0.60
0.5	5550	0	4.27	84.1	0.74
		1	4.99	98.2	0.63

From the estimated velocities, it is apparent that the dominant energy mode (m = 0) pressure fluctuations have a higher computed convection velocity than those in m = 1. Additionally the higher frequency fluctuations have a higher velocity than lower frequency fluctuations. These observations lead to the conclusion that the dominant modes are more important than other modes in determining convection velocity as those will produce more noise since they travel faster.

2.2.4 Convection Velocity from Laser Doppler Velocimetry

Kerhervé et al. [27] demonstrated the use of Laser Doppler Velocimetry (LDV) in the study of a Mach 1.2 screeching cold (TTR = 1) jet to measure convection velocity of a passive scalar. Experiments were conducted at the Centre d'Etudes Aérodyanmique et Thermiques in Poitiers, France. LDV utilizes single-frequency laser light directed into a seeded flow and the Doppler-shifted light is recorded by photomultiplier tubes (PMTs). Using lasers of different wavelengths allows for the capturing three-component velocity measurements within a small volume on the order of less than one cubic millimeter [27]. One of the drawbacks of this technique is that although it is capable of measuring highly time-resolved data (high temporal resolution), this technique lacks the spatial resolution offered by others such as Particle Image Velocimetry (PIV).

Typically LDV is used to measure velocity at a single point, however Kerhervé et al. used a multi-point LDV system in conjunction with specialized correlation techniques to extract convection velocity. As with experiments discussed within prior sections, Kerhervé et al. set one

LDV probe to be stationary while traversing another downstream in small increments. According to the authors, the temporal irregularity of the data can be attributed to the intermittency of particles. To help with issues of this irregular particle distribution, the authors had to use a slotting technique developed by Mayo et al. [28] but adapted for a multi-point LDV system and is described in further detail in Kerhervé et al. [27]. Additionally, the authors additionally needed to reduce the high-variance of the slotting by combing normalization techniques and "fuzzy slotting." Van Maanen et al. [29] combined these techniques and demonstrated that the correlation variance is reduced. After these techniques are applied the two-point correlation can be computed to produce convection velocity.

For this experiment, Kerhervé et al. took convection velocity measurements at five axial stations within the jet plume. For the purposes of the current work, only values for *x/D* of 3, 5, and 6 are presented in Table 2.4 below to add to this catalog of studies on convection velocity.

Table 2.4 Summary of Convection Velocities [27].

Axial Location ***x/D***	**Radial Location** ***r/D***	**Convection Velocity** U_c/U_j
3	0.33	0.89
	0.41	0.81
	0.49	0.63
	0.54	0.56
	0.66	0.46
5	0.23	0.84
	0.36	0.76
	0.48	0.67
	0.57	0.57
	0.77	0.46
6	0.19	0.87
	0.33	0.77
	0.47	0.66
	0.60	0.56
	0.83	0.50

2.2.5 Convection Velocity from Time-Resolved Particle Image Velocimetry

Time-resolved particle image velocimetry (TR-PIV) is a newer laser-based technique developed at NASA Glenn Research Center by Wernet [30]. This system is capable of obtaining measurements at sample rates up to 50 kHz over 2 s with spectral properties up to 12.5 kHz.

Additionally, CMOS cameras are used to capture images of the flow with a base effective sensor size of 1024 x 1024 pixels based on the cameras chosen. At higher frame rates, the effective pixel size is reduced thereby increasing the time-resolution of the system at the sacrifice of spatial resolution.

Two-point correlations for this technique involve taking sub-regions of the larger images and doing multiple passes to find the peak correlation values. This process is done using a program developed at NASA.

High-speed test were conducted by Bridges and Wernet [31] in the Aero-Acoustic Propulsion Laboratory (AAPL) located on the campus of the NASA Glenn Research Center. The main focus of the experiment was to study multi-stream nozzles under both heated and unheated conditions. Additionally, this nozzle differs from previously discussed works in that is contains a center plug; a feature found in most modern aircraft engines. As such, some points within the presented convection profiles will not be considered in the present work where there is clear evidence of this feature causing a depression in the convection profile. Furthermore, for the purposes of the current work, only the case of the single stream jet presented that was operated at Mach 1.48 will be discussed.

Bridges and Wernet acquired data at six axial stations in a Mach 1.48 operated at $TTR = 2.7$ in order to capture data within the potential core, developing shear layer, and beyond the end of the potential core. These locations were $2D$, $3.5D$, $6.5D$, $9.5D$, $12.5D$, and $15.5D$. Data was extracted from the paper and presented in Figure 2.4a, 2.4b, and 2.4c, below, for axial locations that coincide with the current work near the lipline.

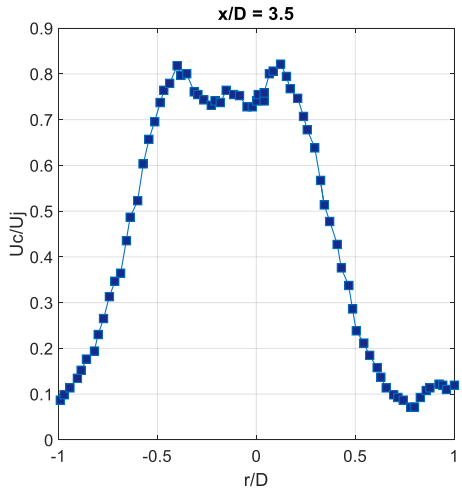

Figure 2.4a Convection velocity profile for x = 3.5D [31].

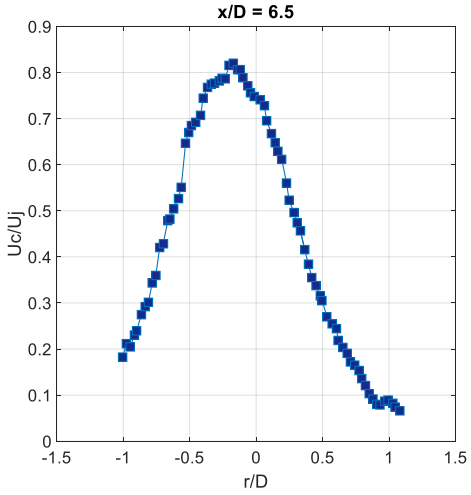

Figure 2.4b Convection velocity profile for x = 6.5D [31].

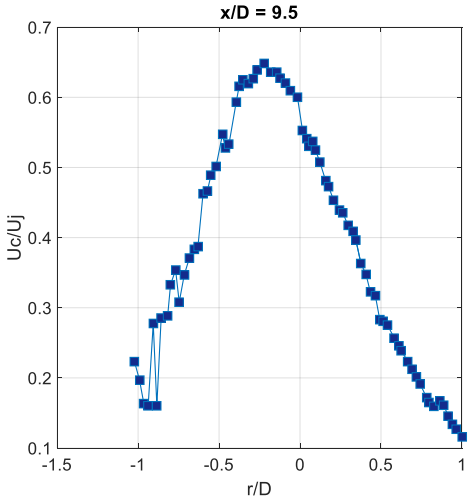

Figure 2.4c Convection velocity profile for x = 9.5D [31].

The authors of this paper also note a few important aspects about the data collected. First, the convection velocity closely resembled the average velocity where there are regions of high turbulence. This is significant because regions of higher turbulence are known to produce more sound. Additionally, the convection velocity matched the average velocity at the location where turbulence was a maximum. Finally, the authors note that for both heated and unheated jets, there was no significant difference between the average velocity and the convection velocity. This fact then becomes of significance when looking at models of jet noise and gives support to the idea of using the average velocity, instead of convection velocity, for estimates.

2.2.6 Convection Velocity from Time-Resolved Doppler Global Velocimetry

Time-resolved Doppler global velocimetry (TR-DGV) is another laser-based technique that is used to non-intrusively measure three-component and convection velocities within the flow. This technique was developed at Virginia Polytechnic Institute and State University by Lowe et al. [32] and matured by Ecker et al. [7]. One benefit to further maturing this system is that it offers the potential to have a higher temporal response than LDV because it does not rely on signals generated by single particles [33]. TR-DGV is described in greater technical detail later, in Section 3.1.

Using TR-DGV Ecker et al. conducted experiments [6, 7, 8, 9] on a military-style nozzle with a design Mach number of 1.65. Two heated jet conditions were studied and compared at four axial stations within the jet plume. These axial stations were chosen to capture the growing shear layer between the potential core and the surrounding medium, as well as to capture the region beyond the potential core. Portions of the data near the lipline presented in these studies has been extracted and summarized in Table 2.6.1 for [7] and 2.6.2 for [8].

Table 2.6.1 Summary of Data for Mach 1.65 Biconic Nozzle [7]

Axial Location *x/D*	Radial Location *r/D*	*TTR*	Convection Velocity U_c/U_j
4	0.5	1.6	0.53
		2.0	0.54
6		1.6	0.59
		2.0	0.56
8		1.6	0.57
		2.0	0.52
10		1.6	0.65
		2.0	0.56

Table 2.6.2 Summary of Data for Mach 1.65 Biconic Nozzle [8]

Axial Location *x/D*	Radial Location *r/D*	*TTR*	Convection Velocity U_c/U_j
4	0.51	1.6	0.57
		2.0	0.57
6		1.6	0.61
		2.0	0.61
8		1.6	0.59
		2.0	0.55
10		1.6	0.67
		2.0	0.57

Through this work, Ecker et al. demonstrated that TR-DGV is a powerful tool capable of capturing convection velocity that is highly time resolved and at multiple locations simultaneously. Convection velocities can be computed from either a filtered signal using gaseous iodine or an unfiltered signal collected from scattered light from a passive scalar in the flow. The filtered signal, however, is composed of a mixture of velocity-based convection velocity due to the physical properties of iodine, and scalar-based convection velocity. In both instances, the convection velocity is likely dominated by the scalar convection speeds and could be validated through a comparison of the resulting velocities for each signal.

Through their experiments, Ecker et al. [7, 8] observed that the convection velocity appeared to increase after the breakdown of the potential core. This region was identified by Hileman and Samimy [34] as a region that significantly contributes to jet noise. Additionally, Ecker et al. [8] noted that a non-monotonic decrease in the convection velocity with increasing radial distance was likely due to the presence of shocks within the flow. These shocks would be a direct result of the nature of the biconic nozzle used during the experiment which had been adapted from the geometry studied by Powers and McLaughlin [39].

2.3 Literature Motivation for Current Work

From the review of past works, it is clear that there are many methods for computing convection velocities. Methods such as shadowgraph imaging and optical deflectometry measure the convective velocity of pressure fluctuations however are limited to observing the outer radii of a jet and are not able to obtain convection velocity of noise producing sources along the jet centerline. LDV, TR-PIV, and TR-DGV all focus on measuring the presence of a passive scalar, which is defined as a seeding particle that moves within a flow but does not change the flow properties when introduced in small quantities, to compute convection velocity.

Figure 2.5 displays a qualitative comparison for the spatial and temporal (or time) resolutions of various flow imaging techniques.

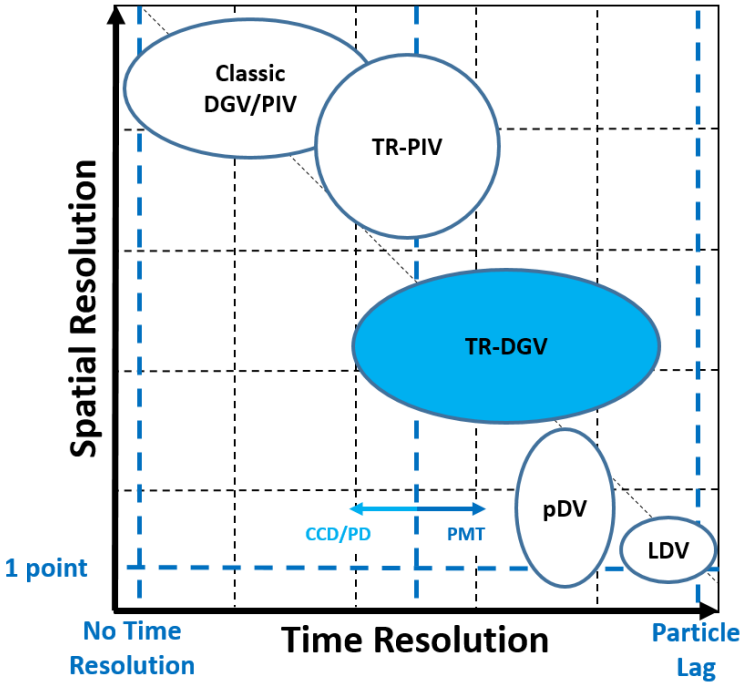

Figure 2.5 Qualitative comparison of imaging techniques

Classical techniques, such as DGV and Particle Image Velocimetry (PIV), have very good spatial resolution and capture a large field of view to obtain mean flow statistics. The limiting component in these techniques is the use of a charged-couple device (CCD) or a photodetector (PD) as a sensor within a camera. Since noise producing eddies can change and develop rapidly,

these techniques are not desirable for measuring convection velocity. TR-PIV greatly improves the ability of PIV by using high framerates to become a useful tool for measuring convection velocity, but still lacks some of the temporal resolution of techniques that utilize PMTs while still maintaining the ability to obtain mean velocities. Techniques such as point Doppler velocimetry (pDV), a technique that is based off DGV but applied at a single point, and LDV lack spatial resolution, but are highly time resolved. These techniques are good at measuring convection velocity but would take much more time to collect a data set that fully investigates the convection velocity throughout the flow. In the case of LDV it can even suffer from particle intermittency. TR-DGV makes up for many of the shortcomings of the aforementioned techniques through the use of PMTs to maintain high time resolution, while using the larger sensor to maintain some spatial resolution by having a larger sensor. It is for these reasons that TR-DGV is used in the current work.

The current work is seeking to expand upon some of the observations made in the above mentioned works using TR-DGV. Firstly, Ecker et al. [8] noted that the data suggested that the data, particularly for the TTR = 1.6 case, demonstrated that the shock cells were causing the convective velocity to decrease non-monotonically. Unfortunately due to the sparseness of axial locations at which data was collected, it was not fully clear if these fluctuations are a result of the shock structure or part of the uncertainty in the technique, which had been calculated through Monte Carlo simulations as being ±6.5% of the local convection velocity. Secondly, Ecker et al. [9] provided a conceptual relationship for the breakdown of the potential core and its influence on eddy convection speeds. Furthermore, the current work seeks to investigate the observation made by Ecker et al. [7, 8] that suggested that a region of increased convection velocity exists beyond the potential core. A full determination of this was also difficult to make due to the sparseness of data taken further downstream of the potential core breakdown.

The current work also seeks to compare convection velocity obtained using TR-DGV with mean velocities obtained using PIV in order to test whether the

3. Methods

The following section describes the experimental setup for the current work using time-resolved Doppler global velocimetry. The first section, Section 3.1, gives an over view of the TR-DGV system developed at Virginia Tech by Lowe et al. [32]. Section 3.2 describes the facility in which the TR-DGV measurements were taken. Section 3.3 discusses relevant geometry and the conditions during the current work. Section 3.4 focuses on methods used to increase the quality of the recorded signal. The main method was the use of free-space optics to help isolate the laser from acoustic interference, this is discussed in Section 3.4.1 while a secondary method is briefly discussed in Section 3.4.2 and involved reducing reflections observed by the PMT sensors.

3.1 Time-Resolved Doppler Global Velocimetry

The current worked uses the Time-Resolved Doppler Global Velocimetry (TR-DGV) technique developed at Virginia Tech. This technique is based off of the Doppler global velocimetry (DGV) technique pioneered by Komine [35] in 1990 and further matured by Komine et al. [36] and Meyers and Komine [37] in 1991. DGV works by taking scattered light from a seeded flow and filters the scattered light through the use of a gaseous vaper cell, in the case iodine, to be detected with some sort of photodetector. The basic method is outlined in Figure 3.1 which was adapted from Komine [35] to add labeling to some of the components.

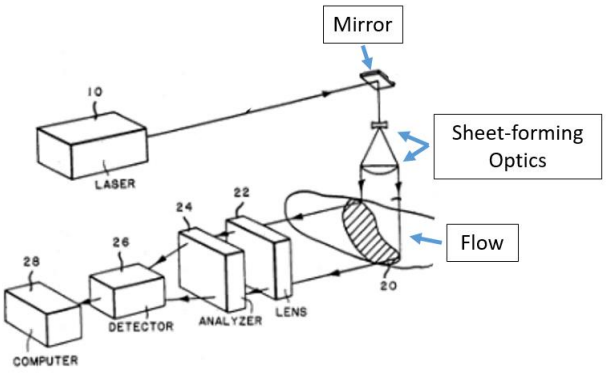

Figure 3.1 Basic Doppler global velocimetry setup adapted from Komine [35]

TR-DGV differs from DGV in that with the use of two Hamamatsu H8500C and two H10660 Photomultiplier Tubes (PMTs) as the “Detectors.” Data from the PMTs is recorded for 1 second

using a customized National Instruments PXIe DAQ system with sampling at 10 MHz. This highly time-resolved data is downsized during post-processing to a signal with a sampling frequency of 250 kHz. Additionally, using the individual pixels of the PMT, the system is capable of obtaining instantaneous three-component velocity measurements at 32 points simultaneously within the flow [7] and is able to be upgraded to obtain 64 simultaneous points [38].

Light for the experiment is provided by a Coherent Verdi V6 532 nm continuous wave laser operated at 6 Watts, is placed in a separate room to isolate it from interference from the noise intensity and frequencies emitted from the supersonic jet. Laser light is directed into the test chamber through a series of mirrors to an optical bench where two Acousto-optic modulators (AOMs), driven by a delay generator, multiplex the beam into two alternating beams which are then directed with mirrors to the traversing measurement setup.

Figure 3.2 shows a 3-D rendering of the traversing setup of the of the TR-DGV system. Not pictured is the traversing unit which is connected to the horizontal cross-piece between the two detector systems. Laser light is received from the nearby optical bench and sent through a cylindrical lens with a focal length of -20 mm.

Figure 3.3 displays the full PMT detector system in detail and highlights the light path in green. These units are typically covered with blackout cloth or enclosed in order to eliminate any ambient light from interfering with the data collection. Additionally, the “Lens and beamsplitter assembly” also includes 532 nm laser line filters to ensure that only reflected light from the flow contributes to the recorded signals from the flows.

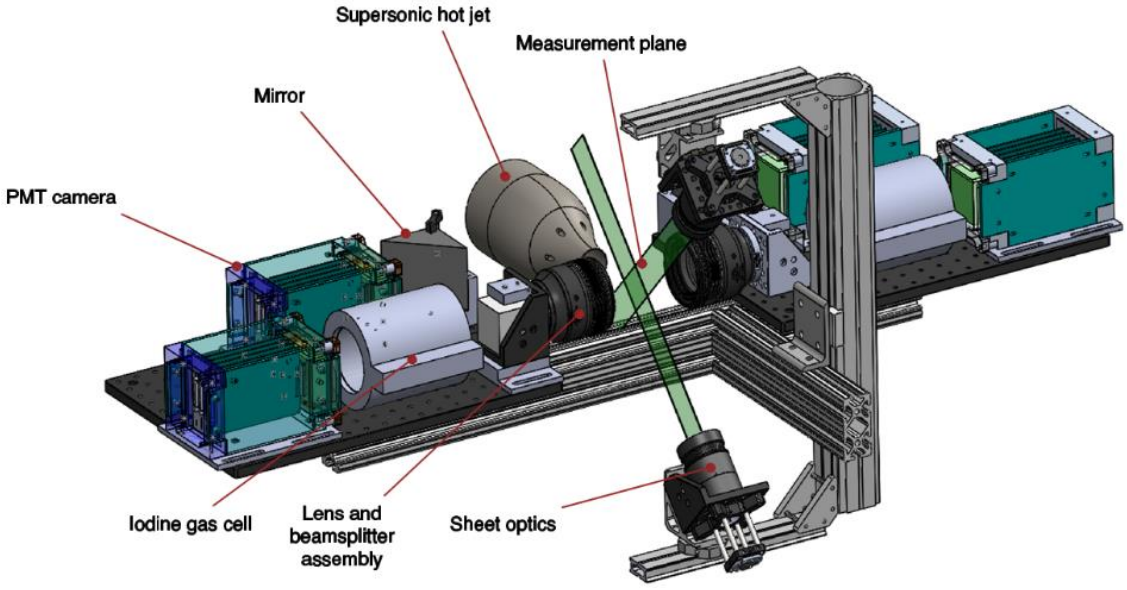

Figure 3.2 Traversing TR-DGV assembly.

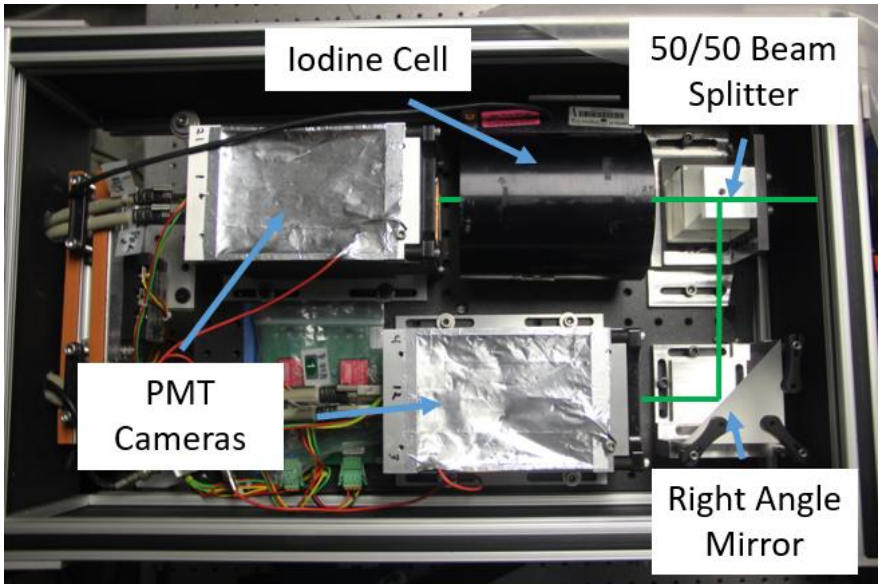

Figure 3.3 PMT detector system. Light path in green.

3.2 Facility Overview

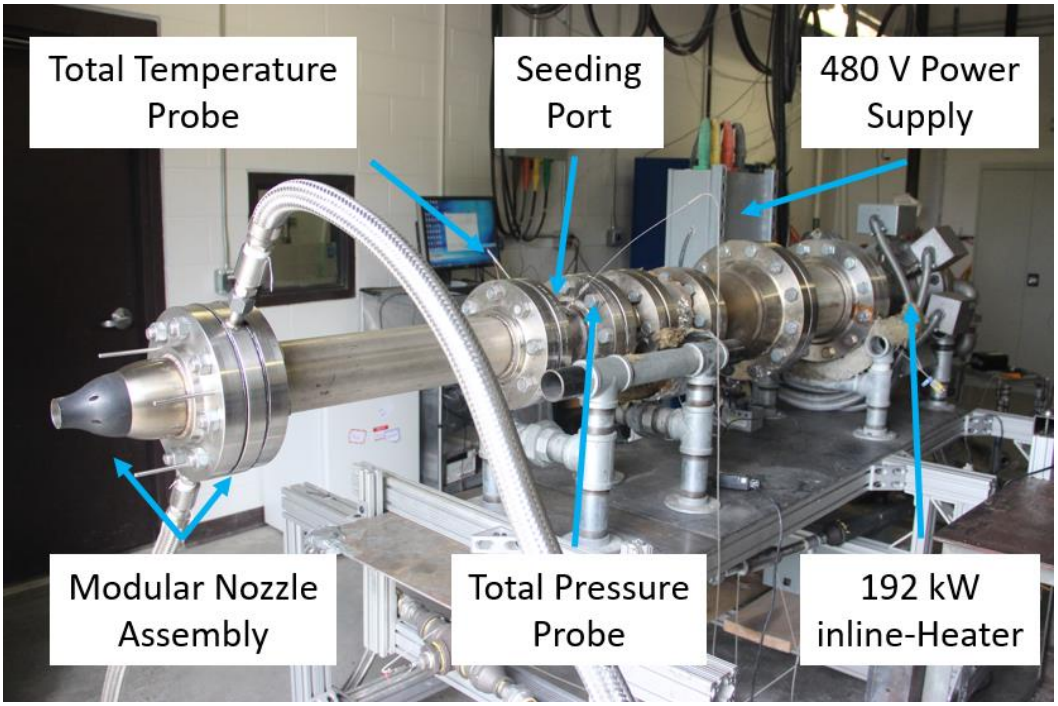

Figure 3.4 The Virginia Tech hot supersonic jet facility

The current work on unheated supersonic jets was conducted in the Virginia Tech hot jet facility, shown in Figure 3.4, within the Advanced Propulsion and Power Laboratory. This laboratory has previously been described by Ecker et al. [8] with the modular jet assembly described in detail by Mayo et al. [11] which allows for the easy transition between the studies of different geometry nozzles. Pressurized air is provided from a compressor with a maximum pressure of 175 psi. Pressurized air is then sent through a 192 kW inline heater capable of generating a TTR up to 3.0. Flow is then sent into a mixing chamber to ensure that the temperature of the flow is evenly distributed before moving through flow straighteners and to the nozzle modular nozzle assembly.

One experiment conducted for the current work used a biconic nozzle (depicted later in Figure (3.5)), with design Mach number M_d equal to 1.65 with an exit diameter of 38.1mm. This nozzle was previously used in heated experiments, such as those described by Ecker et al. [7, 8, 9], and is an axisymmetric adaptation of the geometry studied by Powers and McLaughlin [39] for military-style nozzles. This experiment also used 1 μm diameter Titanium Oxide particles

introduced far upstream of the nozzle exit in the plenum through the labeled seeding port in the above figure to ensure even mixing within the flow.

Additionally, data was obtained with a nozzle designed using the contoured designed for a Mach number of 1.5. Detailed information on this nozzle can be found in Mayo et al. [10] for work on pressure distortions. It was noted that the nozzle was poorly manufactured and contained visible groves from the milling process thereby making the nozzle produce a plume containing shocks. This nozzle also has an exit diameter of 38.1 mm and the flow was also seeded with the same particulate as the Mach 1.65 study.

3.3 Experimental Parameters

The current work focused on collecting data at several axial stations downstream of the nozzle exit. These stations ranged from $x = 3D$ to $x = 13D$ from the nozzle exit with a station located at $0.5D$ intervals apart, note that $x = 0D$ represents the location of the nozzle. These locations were chosen to ensure a greater resolution of structures that may be in the flow, particularly shock cells. Due to geometric limitations between the nozzle and laser sheets, it was not possible to obtain data closer than $3D$ without contaminating the recorded signals with scattered light from the nozzle. Figure 3.5 displays the geometry of the laser sheets (in green) relative to the nozzle. The PMT sensor location is also displayed by the red grid. For the current work, the observed region extends from the jet centerline at $r \approx 0D$ to $r \approx 0.6D$ or just below the lipline ($r = 0.5D$) in order to ensure that the growing shear layer was observed during the experiment.

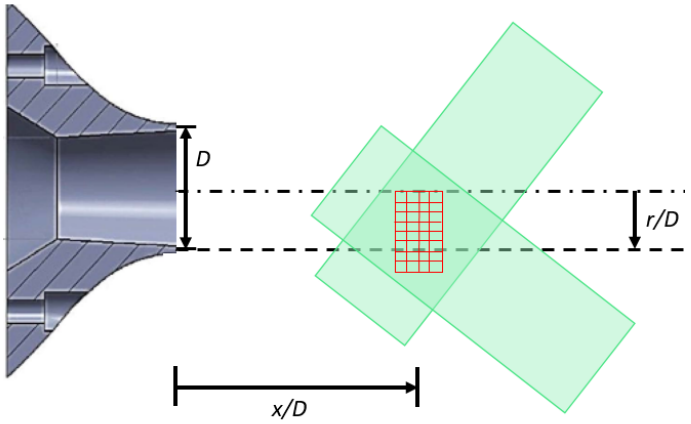

Figure 3.5 Measurement configuration

Table 3.1 below summarizes relevant flow parameters for the current work. The top three rows pertain to the work with the biconic geometry nozzle with *TTR* = 1 and also the parameters studied by Ecker et al. [8] for the work on flows of *TTR* = 1.6 and *TTR* = 2.0. The later cases are mentioned here for the reader as these cases are compared to the *TTR* = 1 case in Section 4. The fourth row summarizes relevant flow parameters for the current work using the contoured nozzle with *TTR* = 1.83 and a Mach number of 1.48.

Table 3.1 Experimental Parameters Current Work

Nozzle Type	*TTR*	M_j	*Re*
Biconic	1	1.65	2.55M
	1.6	1.68	1.3M
	2	1.7	1.15M
Contoured	1.83	1.48	946K

3.4 Measures to Improve Data Quality

This section discusses the methods taken to increase the signal-to-noise ratio of the data collected for the current work. Section 3.4.1 will discuss the use of free-space optics and Section 3.4.2 will touch on how the impact of reflections was mitigated.

3.4.1 Free-Space Optics

Previous experiments conducted by on heated jets used fiber optics in order to deliver the laser light to the measurement region of the flow. Using fiber optics severely limits the amount of laser power that can be transmitted to well less than 1 Watt of power. For the current work, it was desired to increase the power output of the Verdi laser used in order to obtain a higher signal-to-noise ratio. In order to achieve this goal and to isolate the laser from noise, a free-space optics design was used to transport the laser beam from the control room of the hot jet facility into the test cell. The laser was placed inside of the control room of the hot jet facility, with no direct path for sound to travel from the jet to the laser. This was done since it was overserved in other experiments that having the laser in the same room as the jet caused the laser frequency to become unstable and incapable of yielding usable data. Figure 3.6 below shows the setup of the free-space optics on the optics bench within the jet test cell.

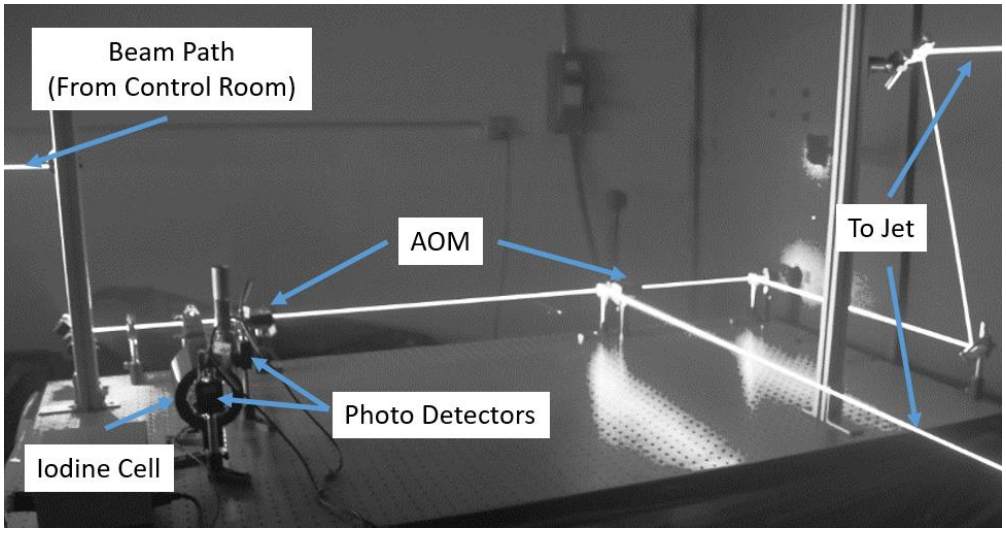

Figure 3.6 Optical bench during experiments

As labeled in the figure above, the beam path comes from the control room from the left of the figure. The light is then split and a weak beam is passed through reference optics into two photo detectors with 532 nm filters. These filters act to only allow the wavelength of light produced by the laser to reach the photodetector. Two acousto-optic modulators (AOM) are operated to pulse the beam with a frequency of 250 kHz. The laser is then sent toward the jet out the right side of the photo. The resulting beam power before the beam is directed into sheet-forming optics is approximately 1.1 W per beam.

3.4.2 Reflection Mitigation

Additional care was also taken into account for limiting the number of reflections that could interfere with the recorded data. Several actions were taken in order to reduce reflections and are displayed in Figure 3.7 below. Reflections were mostly apparent off of the nozzle itself. To mitigate these, flat black gaffers tape or flat black spray paint was used on the outside of the nozzle was used. Some minor reflections still existed from the inside of the nozzle, but this was not painted or tapped as not to affect the inner geometry of the nozzle. Additionally, cloth was used to cover much of the jet to reduce any light coming from the upstream sections of the jet. Orange tape and flat black spray paint was used to reduce reflections from the 80/20 structure. The orange tape, although it reflects bright light serves primarily to change the wavelength such that it is not absorbed by the 532 nm filters on the lenses of the cameras. A final method for mitigating reflections was to place a sheet of plywood painted flat black above the experimental

setup to terminate the laser sheet so that the laser would not reflect off of the white ceiling in the test cell.

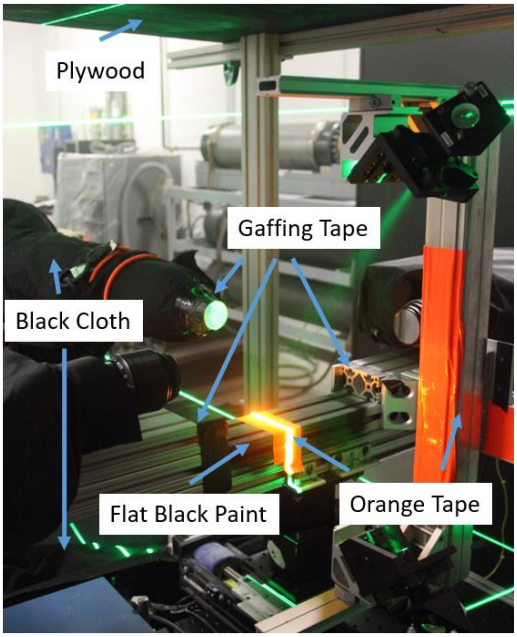

Figure 3.7 Reflection Mitigation

3.5 Computing Convection Velocity

Convection velocity can be calculated using the second-order two-point cross-correlation displayed in Equation (3.1). The overbar in the latter portion of the equation denotes that the resulting value is time-averaged.

$$R_{ij} = \frac{1}{T}\int_{-\frac{T}{2}}^{\frac{T}{2}} s_i(x,r,t)s_j(x+\Delta\varsigma, r+\Delta\xi, t+\Delta\tau)dt = \overline{s_i(x,r,t)s_j(x+\Delta\varsigma, r+\Delta\xi, t+\Delta\tau)} \quad (3.1)$$

In order to apply this equation, the signal obtained from the scattered light of the passive scalar consisting of 250 thousand laser pulse pairs with a large pause between pairs and a small pause in between laser pulses must be reduced from the collected PMT signal. An example of this raw signal is displayed in Figure 3.8a.

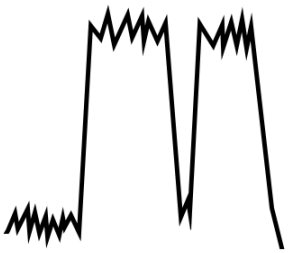

Figure 3.8a Example of recorded PMT signal

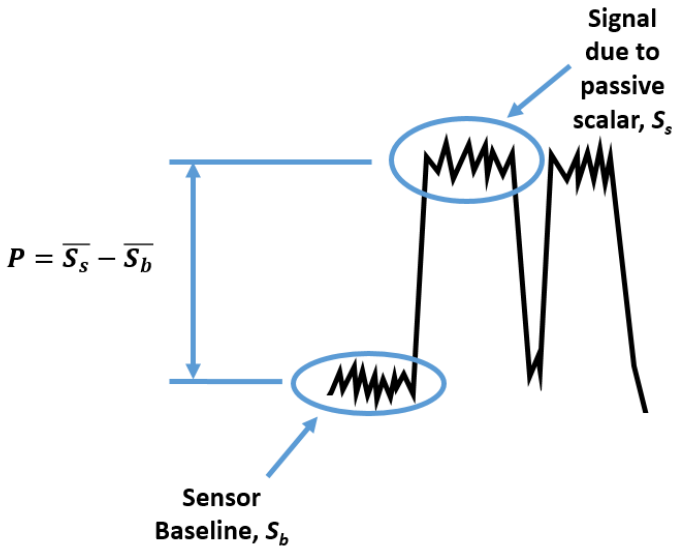

Figure 3.8b Example of signal due to passive scalar

The portion of the signal that is due to the noise inherent in the PMT sensor S_b and the recorded signal due to the light collected from the passive scalar S_s, depicted in Figure 3.8b, are respectively averaged and subtracted to yield an amplitude P proportional to the local concentration of the passive scalar, assuming uniform seeding. This operation results in a vector of length N, where N is the number samples, and is displayed in Equation (3.2).

$$\boldsymbol{P} = [\,(\overline{\boldsymbol{S_s}} - \overline{\boldsymbol{S_b}})_{\boldsymbol{1}}\,,(\overline{\boldsymbol{S_s}} - \overline{\boldsymbol{S_b}})_{\boldsymbol{2}}\,,\ldots\,,(\overline{\boldsymbol{S_s}} - \overline{\boldsymbol{S_b}})_{\boldsymbol{N-1}}\,,(\overline{\boldsymbol{S_s}} - \overline{\boldsymbol{S_b}})_{\boldsymbol{N}}\,] \qquad (3.2)$$

Next, using Equation (3.1), the amplitudes of two pixels, P_1 and P_2, are cross-correlated for this specific application using Equation (3.3).

$$R_{12} = \frac{1}{T}\int_{-\frac{T}{2}}^{\frac{T}{2}} P_1(x_1, r, t)P_2(x_1 + \Delta x, r, t + \Delta\tau)dt = \overline{P_1(x_1, r, t)P_2(x_1 + \Delta x, r, t + \Delta\tau)} \quad (3.3)$$

Correlations are performed between the individual pixels of the PMT sensor within the same row to yield a peak correlation lag time $\Delta\tau$ which is interpolated using a cubic spline due to the method's low error compared to other methods as discussed by Ecker et al. [8]. Correlations are performed between non-adjacent pixels to yield three values for the lag time in order to compute three convection velocities. Adjacent pixels are not used because correlatons between these pixels closely represent an auto-correlation or yield a lag time that results in convection velocities in excess of $5U_j$.

$$U_c = \frac{1}{N}\sum_{j=1}^{N} U_{c,j} \quad (3.4)$$

$$U_{c,j} = \frac{\Delta x_j}{\Delta\tau_j} = \frac{\Delta p_j}{\Delta\tau_j * M} \quad (3.5)$$

These three convection velocities are then averaged to obtain a mean convection velocity for a specific axial and radial location in the flow using Equation (3.4) with *N* equal to 3. The individual convection velocities are calculated using Equation (3.5) where Δx_j is the physical real-world space observed between correlated pixels, and is equivalent to Δp_j, the phyical spacing between pixels on the PMT, divided by a magnification multiplier *M* which has units of pixels per meter.

3.5.1 Repeatability of Measurements

In order to quantify the repeatability and random error of the measurement and computations, a two-sided Student's t-distribution with 95% confidence was applied to the standard error equation shown in Equation (3.6).

$$\delta U_{c,std} = t * \frac{\sigma_{U_{c,j}}}{\sqrt{N}} \quad (3.6)$$

$\delta U_{c,std}$ is the standard error of the convection velocity, *t* is the t-statistic, *N* is the sample size of velocities at a location, and $\sigma_{U_{c,j}}$ is the standard deviation of the convection velocity samples.

This standard error was typically much greater near the nozzle exit and near the centerline compared to further downstream of the nozzle exit. For the heated Mach 1.48 data, the maximum standard error was $\pm 0.39U_j$ and a mean standard value of $\pm 0.03U_j$. The unheated Mach 1.65 data had a maximum standard error of $\pm 0.57U_j$ with a mean standard error of $\pm 0.04U_j$. It should be noted, however, that the unheated data, which was a better quality data set in terms of outside interferrence (discussed later in the results section), only appears to have a higher maximum standard error because normalized convection velocities greater than 1.1 were excluded from the presented data due to the fact that these values are inherently unrealistic; the convection velocity theoretically cannot be greater than the exit velocity. If all velocities are included, the maximum standard error for the heated case would be $\pm 24U_j$ with a mean standard error of $\pm 0.29U_j$, whereas the standard error values for the unheated case remain unchanged.

4. Results

The following section documents the results of the experiment conducted on the Mach 1.65 biconic nozzle operated at *TTR* = 1. The focus of the current work was to determine whether a non-monatomic decrease observed in the convection velocity in past works [8, 40] on this nozzle geometry is caused by shock cells within the core of the jet. Additionally, the current work looks to find evidence of what was noted by Ecker et al. [7, 8] that there is a region beyond the potential core with an increase in convection velocity. The first section discusses a comparison of past unheated measurements to the current work. Section 4.2 will cover results comparing the current work on unheated biconic jets to the past works on this nozzle geometry, as well as discuss the work of using shadowgraph imaging to verify shock location within the plume. Section 4.3 will discuss contours of the collected convective velocity data and look at the convection velocity observed beyond the end of the potential core. Finally, Section 4.4 will present a comparison of convection velocity with average velocity from PIV data taken on the same nozzle geometry and under the same conditions.

4.1 Comparison of Unheated TR-DGV Measurements

As mentioned in Section 3, TR-DGV data was collected on a Mach 1.65 unheated flow emanating from a biconic nozzle. Since there have been a number of other investigations of convective velocity in cold jets, the current data will be compared to those results at constant radial locations within the jet plume near the lipline of the jet ($r = 0.5D$).

Because of the magnification of the interrogation region and the limited pixels available on a PMT sensor, data for the current work was not obtained exactly at the lipline and is instead presented for the two available locations near the lipline of the jet; $r = 0.46D$ and $r = 0.54D$. Results are presented in Figure 4.1 and are compared with data from other research groups.

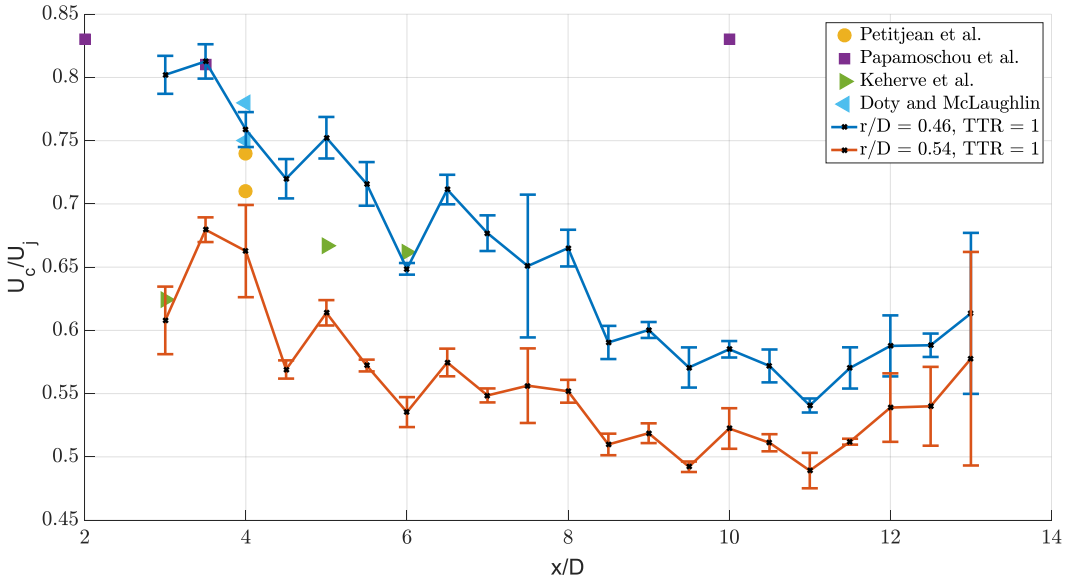

Figure 4.1 Normalized convection velocities plotted vs. axial location *x/D* for data near the lipline.

The data in the current work, denoted by the blue and red points, are compared with the unheated data presented by Petitjean et al. [23], Papamoschou et al. [24], Kerhervé et al. [27], and Doty and McLaughlin [22]. All of the data sets presented are taken near the lipline of the jet within $r = 0.04D$ of the jet centerline. Additionally, the work by Papamoschou et al. was conducted on a Mach 1.75 flow, leading to the higher non-dimensional convection velocities compared to the other data sets. What is interesting, is that all of the past works conducted by Petitjean et al., Papamoschou et al., and Doty and McLaughlin used optical deflectometery as the basic method

for obtaining convection velocity. Both the data for the current work and the work by Kerhervé et al., which rely on seeding to represent the flow, display comparable non-dimensionalized values for the convection velocity near the nozzle exit, within the developing shear layer. For the current work, the convection velocities ranged between $0.61U_j$ and $0.80U_j$ near the nozzle exit and decreases to a minimum between $0.49U_j$ and $0.54U_j$ near the breakdown of the potential core which is estimated at approximately $11D$ using the method described by Witze [42] for a perfectly expanded flow. In the paper by Witze, multiple experimental results were used to test previous theories of potential core length, with a focus on the work of Kleinstein [44]. Based on this model, Witze further improved upon the model so that it accurately predicted the experimental resulting centerline obtained from subsonic and supersonic experiments operated at various heated and unheated conditions.

As noted previously by Ecker et al. [8] and Shea et al. [40], it is presumed that the non-monotonic decrease in the convection velocity seen in the data obtained using TR-DGV is due to the presence of shock cells within the jet plume resulting from the biconic geometry of the nozzle. This will be discussed in further detail in Section 4.2.

4.2 Shocks and Convection Velocity

Ecker et al. [8] first noted a non-monotonic decrease in data collected on the same nozzle used in the current work. This data was only collected at four axial stations within the jet plume with two locations in the potential core, one at the end of the potential core, and one in the region beyond the breakdown of the potential core. Due to the sparseness of the data, it was difficult to discern the full effect of the shock structure within the jet. The current work and the work by Shea et al. [40] expands upon this by obtaining data at axial locations with smaller changes in axial location of the interrogation window and by collecting shadowgraph images.

Figure 4.2 displays data near the jet lipline for the current work on heated and unheated jets, as well as the two cases studied in Ecker et al. [8] (Mach 1.65 at $TTR = 1.6$ and $TTR = 2.0$). From this figure, it is clear that the data presented for the current work, in red and blue, does not monotonically decreases, and the data for Ecker et al. increases, decreases, and increases again as

the interrogation window moves downstream. The same is true for the current work on the contoured nozzle, as it contains some shocks.

It should, however, be noted that this hot jet data was filtered using a 12^{th} order low-pass Butterworth filter. During processing, it was discovered that there was the presence of a tone on the order of 10^5 that was adversly affecting the correlation of signals. This filter was desinged with a 50% cut-off so that it did not affect the low-frequency range associated with jet-noise. Even after filtering the data, a sensible convection velocity was not able to be calculated near the edge of the interrogation window at near the centerline between $x = 3D$ and $x = 5D$, and at a couple radial locations at $x = 8.5D$.

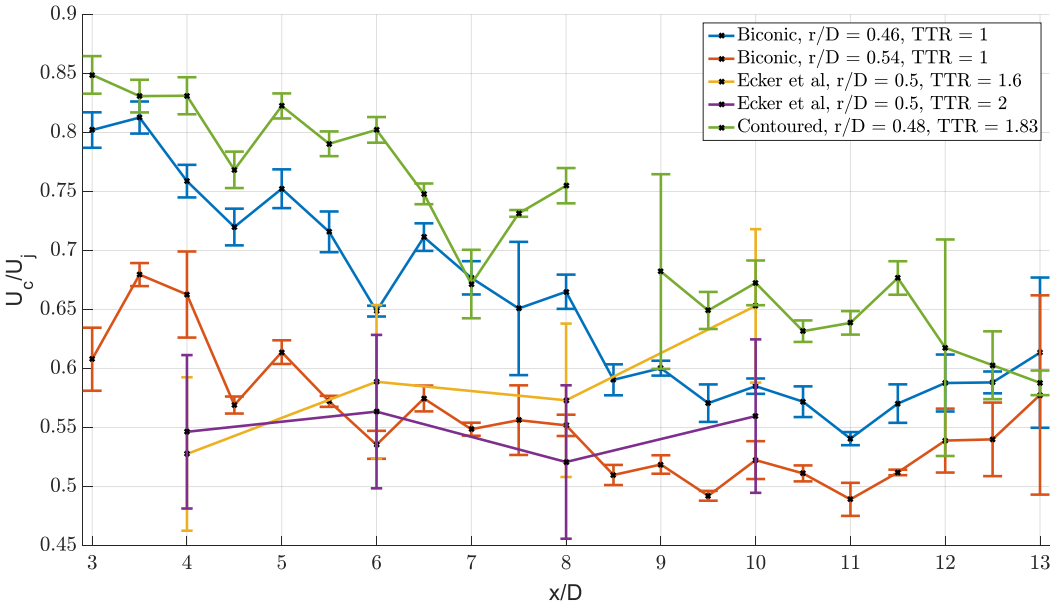

Figure 4.2 Convection velocity near the lipline for heated and unheated TR-DGV data.

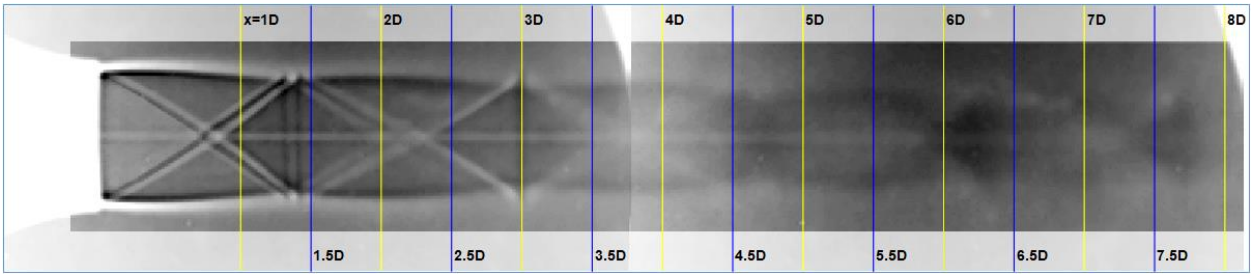

Figure 4.3a Composite Shadowgraph images for Mach 1.65 *TTR* = 1 experiment. Axial locations are marked from $x = 1D$ to $x = 8.5D$ in half diameter increments.

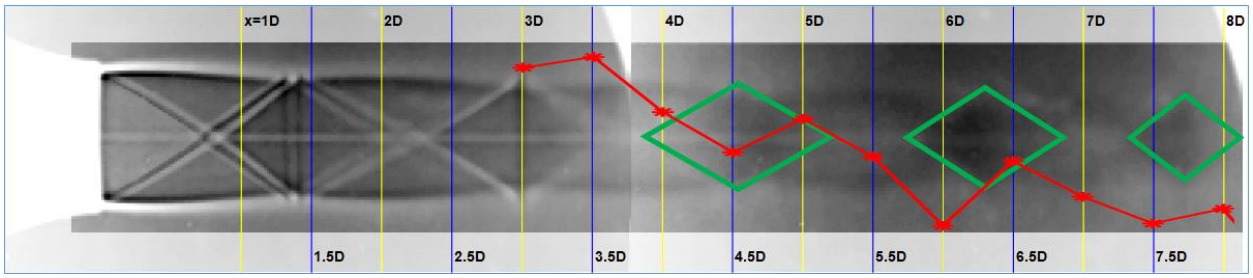

Figure 4.3b $r = 0.54D$ data overlayed to show example data relative to shock structure. Shock diamonds are highlighted in green for convenience.

Figures 4.3a and 4.3b display the results obtained in the current work collected using a shadowgraph system to visualize the shock structure within the jet. Figure 4.3a gives the reader an idea of the greater flow field in the plume with distances marked in increments of $x = 0.5D$. Shocks are very pronounced near the nozzle exit and become less obvious downstream due to weaker shocks and the potential of small alignment errors during the test. Images were taken throughout the same domain as in the TR-DGV experiment; however, the figure has been cropped for purposes of visualizing.

Figure 4.3b depicts data from Figure 4.2 for the case of $r = 0.54D$ is overlaid for visualization of the increasing and decreasing convection velocity relative to the shocks. It should be noted that while the data is aligned with the correct axial location, it is not aligned with its proper radial location. Shock cells have been highlighted for ease of explaining without overcomplicating the figure.

Between the shock cells shown in Figure 4.3b, there is an expansion and a compression within the flow before reaching the next shock diamond. This expansion/compression is more apparent in Figure 4.3a near the nozzle exit. As is well taught in standard high-speed and compressible aerodynamics courses, expansions in high-speed flows are accompanied with accelerations of an air flow and compressions are associated with a deceleration in flow speed. From the figure, it is fully clear that the expansions and compressions align with the increases and decreases in convection velocity observed in the data of the current work and previously presumed by Ecker et al. [8].

4.3 Convection Velocity Beyond the Potential Core

Ecker et al. [7, 8, 9] also noted that there appeared to be an increase in the convection velocity after the breakdown of the potential core in the jet. This increase in convection velocity can be seen in Figure 4.2 above, where in the heated Mach 1.65 data the potential core ends at $x = 8D$ and in the current unheated work at $x \approx 11D$, however the convection velocity continues to rise.

To better visualize this, Figures 4.4 and 4.5 display contours of two data sets obtained with TR-DGV for the current work. Figure 4.4 is of the unheated Mach 1.65 jet and Figure 4.5 is data taken from a Mach 1.48 flow emanating from a contoured nozzle operated at $TTR = 1.83$.

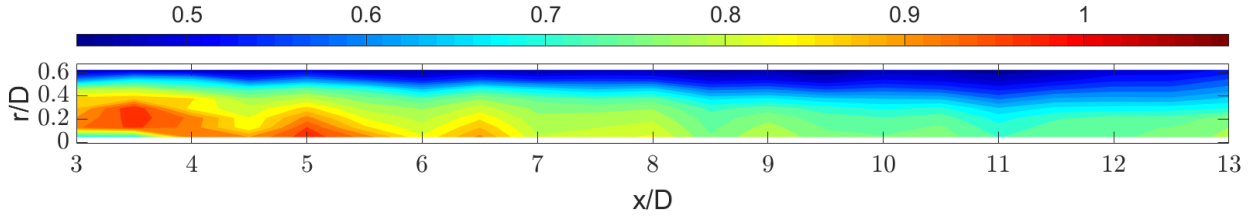

Figure 4.4 Filled contour of normalized convection velocity for Mach 1.65 unheated flow.

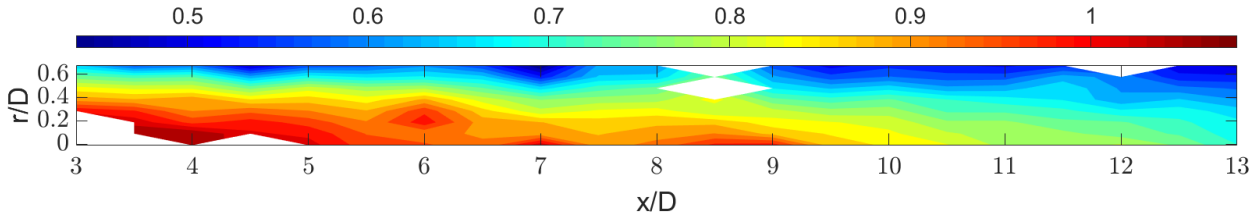

Figure 4.5 Filled contour of normalized convection velocity for Mach 1.48 heated flow.

In Figure 4.4, the end of the potential core is estimated to be x ≈ 11D. It should be noted that at this location, the convection velocity along the centerline ($r = 0D$) has fallen below $0.73U_j$. Additionally, the mean radial convection velocity is at a minimum $0.63U_j$. Further downstream, the convective velocity increases throughout the remaining domain of the data obtained. This is consistent with the hypothesis described by Ecker et al. [9] where the breakdown of the potential core causes high-momentum eddies to convect downstream and add to noise in that region. However, it is possible that the increase in the conveciton velocity is due to the presence of another shock interaction. From the contour, between $x = 11D$ and $x = 13D$, the pattern of expansions and compressions is not apparent and a high-quality shadowgraph or other flow

visualization would be beneficial in determining how far the shock structure propagates downstream of the nozzle exit.

For the case of the heated jet in Figure 4.5, the potential core is estimated to end at approximately $x \approx 7.4D$ based on the method described by Witze [42]. Unlike the unheated data obtained with the biconic nozzle, the heated contoured nozzle data does not have the same minimum in the average radial convection velocity. Along the centerline, the convection velociity periodically increases and decreases out until $x = 9.5D$. This leads to the idea that the shock structure may persist out to this location, however, without flow visualization, it is not possible to determine if this is the case. Beyond $x = 9.5D$, the centerline velocity decreases to a minimum convection velocity of $0.71U_j$ at $x = 13D$. From data presented in the following section (Section 4.4). mean velociity obtained using PIV shows that for a Mach 1.5 jet operated with $TTR = 1.87$, the potential core ends at $x \approx 7.7D$. A flow that is mildly slower and mildly cooler, yet overall has very similar flow characteristics to the faster and hotter flow, should have a similar potential core length. Based on this, the centerline convection velocity at the estimated end of the potential core for the unheated data ($0.73U_j$), and the location of the minimum convection velocity of the heated data presented in Figure 4.5, it can be said that there does not appear to be a universal convection velocity which denotes the end of a potential core.

Furthermore, in Figure 4.5, there is not a clear increase in the convection velocity after the estimated termination of the potential core. This then begs the question wether the increased convection velocity seen in the unheated data presented in Figure 4.4 and seen in the data from Ecker et al. [7, 8, 9] is due to the breakdown of the potential core or if it is a result of the biconic nozzle geometry used during the experiments.

4.4 Comparing Average Velocity and Convection Velocity

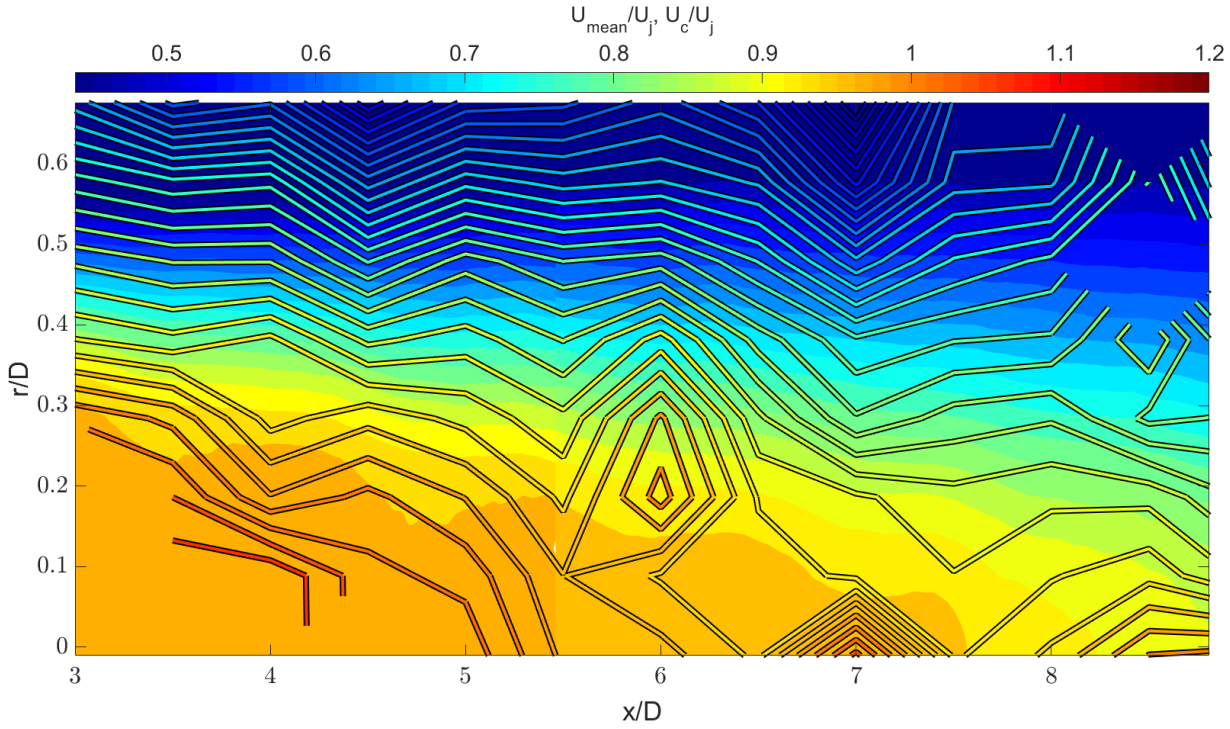

Figure 4.6 Pseudocolor contour of average velocity obtained with PIV at *TTR* = 1.87 and contours of convection velocity from TR-DGV on contoured nozzle at *TTR* = 1.83.

PIV data was provided for the entire flow-field of the contoured nozzle operated at Mach 1.5 with *TTR* = 1.87 by David Mayo at Virginia Tech for comparison with the convection velocities from TR-DGV. Figure 4.6 displays a section of the PIV data obtained between $x = 3D$ and $x = 8.8D$ with the heated Mach 1.48 data overlayed with an equvalent contour level for both data sets. From this figure, it is clear that the convection velocity is higher in the developing shear layer than the average velocity. Aside from a couple of locations where the standard error is large compared to the mean standard error discussed in Section 3.5.1, the convection velocity is lower than the mean velocity. These findings are inline with the findings of Kerhervé et al. [27] and Morris and Zaman [41] where the mean velocity is higher near the centerline than the convection velocity and lower than the convection velocity further into the shear layer. This is also counter to the conclusions made by Bridges and Wernet [31] that the convection velocity is a good approximation of the convection velocity especially within the shear layer.

Figure 4.7 displays this comparison between the mean velocity from PIV and convection velocity from TR-DGV of the heated data obtained from the contoured nozzle. At x = 6.5D, for radial locations less than 0.25D, the convetion velocity is lower than the mean velocity, while at higher radial locations, the convection velocity is higher than the mean velocity. For this axial location, the average standard error is 0.01U_j. With low standard error and in finding similar results to Kerhervé et al. [27] and Morris and Zaman [41], the results of the current work do not reflect those of Bridges and Wernet [31] that the mean velocity is a good approximation of the conveciton velocity.

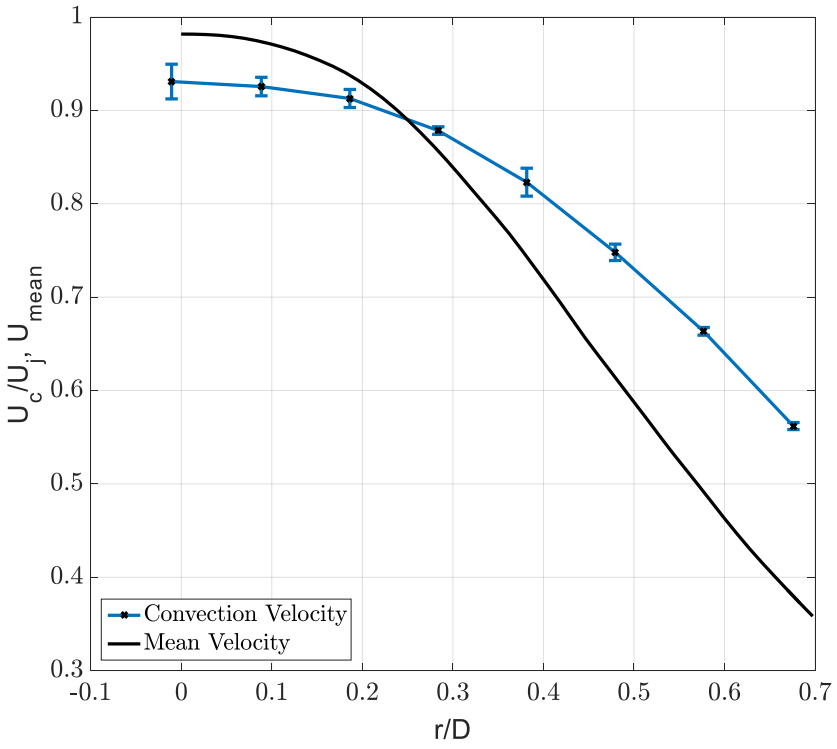

Figure 4.7 Mean velocity and convection velocity profiles at x = 6.5D.

5. Discussion

Although the current work succeeded in obtaining data sets for both hot and cold jets with higher resolution than previous experiments, more work can be done using TR-DGV to investigate convection velocity in a jet. One of the limitations in the current work was the limited radial distance over which data was taken. Figures 4.4 and 4.5 showed contours of the convection velocity over the entire region investigated in the current work. It is apparent in both figures that

the radial span of the interrogation window did not capture much of the growing shear layer further away from the jet centerline. Additionally, in Figures 4.4 and 4.5, the effect of shocks further into the shear layer was, in the opinion of the author, not adequately studied due to a lack of data in that region. Obtaining TR-DGV data out to the ambient air would allow for the study of how the shock structure within the potential core impacts the shedding of irrotational fluid along the length of the potential core as described in Ecker et al. [9]. This could be accomplished by using either larger interogation windows at the cost of resolution, or using a smaller interogation window at the cost of taking data sets at more locations. Of these two methods, a smaller interrogation window may be prefered due to the rapidly changing nature of the shear layer.

From figures presented in Sections 4.1 thru 4.3, it is also clear that there is some increase in the convection velocity after the breakdown of the potential core for the biconic nozzle. Without the clear observance of the increased region of convection velocity, it is unclear if this is a result of the breakdown of the potential core as posed by Ecker et al. [9]. Since this increased convection velocity was only observed in the data obtained using the biconic nozzle, it is possible that this is only a result of the nozzle geometry. To further test this, obtaining convection velocity on the contoured nozzle under unheated conditions would be required, thus eliminating the variable of heat. Additional experiments could be done with other nozzles, like a nozzle designed using the Method of Characteristics, to further test the idea that this is solely based off of the nozzle geometry. Additionally, flow visualization would also be beneficial for seeing if this increase in convection velocity is due to the presence of shocks in the area of interest.

A third area to focus on is seen in some of the data sets collected for the current work and its results. In Figures 4.5, and 4.6, there are portions of the results that yielded normalized convection veloities greater than a value of 1, which is not a logically correct result given that the packets of air can not be moving faster than the jet exit velocity. These results are most likely due to small interferences with the TR-DGV system, specifically with the stabilization of the laser frequency, while collecting data. Despite efforts to mitigate ambient reflections contaminating data, it is possible that some reflections were not suppressed from the laser hitting the inside of the nozzle when near the nozzle exit. These reflections could lead to correlations between sensors having a shorter lag time, resulting in a higher convection velocity. Two options

to mitigate this would be to, first, upgrade to the full capability of the system as described by Ecker et al. [38], and, secondly, to better control and direct laser light to the experimental setup. The former option, would allow for the use of the entire sensor for computing the convection velocity. It also give the chance that reflected light with not be observed by the entire sensor. Better control and better laser routing would help by reducing the possibility of having any reflections. This could be accomplished through using a laser sheet that is not as wide or is of constant width. Reducing the number of mirrors required to direct the laser to the experimental setup would also benefit the system as it would allow for more laser power to reach the setup (better signal-to-noise ratio) and cut down on amient reflections. A final note on improving data collection is to do on-site processing of the power spectra of the raw data. During processing of the data for the contoured nozzle, it was discovered that several frequencies were interfering with the recorded data, which had an impact on the computed convection velocities. Although most of these issues can be solved using a filter, it is preferable to identify the source of the frequency and mitigate its effects during testing, rather than during data processing. Another possibility is that these high convection values could partially be due to errors in determining the image magnification. This could be solved by placing a point light source of known size within the interrogation window and measuring its size on the PMT sensor.

A final item of interest to the author would be to simultaneously obtain PIV and TR-DGV data. This would allow for a better comparison of the two data sets and determine what regions of the flow would be appropriate for using the mean velocity to approximate the convection velocity beyond the region of the shear layer with high turbulence as discussed by Bridges and Wernet [31].

6. Conclusions and Summary

For this work, data was collected and presented on both a Mach 1.65 unheated flow and a Mach 1.48 heated flow operated at $TTR = 2$. Upon comparing the data collected with TR-DGV on the unheated Mach 1.65 jet to experiments on other unheated jets using other techniques, such as OD, TR-PIV, etc., it was clear that there was good agreement of non-dimensionalized convection velocity between cases. Additionally, it was apparent that the geometry used in the current work

exhibited signs of shocks within the flow-field along the lipline; something that was not present in the other datasets.

From comparing the unheated and past heated work on the Mach 1.65 biconic nozzle, it was clear that there was a non-monotonic decrease in the convective velocity at further axial stations from the nozzle exit. Shadowgraph imaging was used in order to qualitatively verify the location of shock structures within the jet plume. It was conclusively found that with the increased resolution of data points and their alignment within the shadowgraph images, that the expansions and compressions caused respective accelerations and decelerations of the local convection velocity.

Additionally, evidence was presented to support the idea that high-momentum eddies are shed by the potential core downstream and contribute to noise within that region; however without clear flow visualization in this region, it is not clear if this is caused by a continuation of the shock structure or by the hypothesized shedding effect presented by Ecker et al [8]. It was also noted that this effect was only observed in the data obtained using the biconic nozzle and not the contoured nozzle. This lead to the question of whether this increase in convection velocity after the breakdown of the potential core is only a result of the nozzle geometry.

It is in the opinion of the author that more work should be done to study the region beyond the potential core to assess the convection velocity of eddies within this region and how they develop. Additionally, it is believed that the interaction between shocks in the potential core and convection velocity should be studied further away from the jet centerline. Unfortunately, the present work did not capture as much of the flow-field and shear layer to adequately identify how far into the shear layer the shocks impact the convection velocity. These future tasks can be done by using a larger magnification within the flow but at the cost of needing to take more measurements in the radial direction.

References

[1] United States, Veterans Affairs. (2017). *Annual Benefits Report - FY2016*(pp. 1-52). Retrieved August 22, 2018, from https://www.benefits.va.gov/REPORTS/abr/ABR-Compensation-FY16-01262018.pdf.

[2] Tinnitus. (2018, March 03). Retrieved August 22, 2018, from https://www.mayoclinic.org/diseases-conditions/tinnitus/symptoms-causes/syc-20350156

[3] Keefe, S. (2015, February 27). F/A-18 Program Explores the Use of Exhaust Nozzle Chevrons to Reduce Engine Noise. Retrieved August 22, 2018, from http://navysustainability.dodlive.mil/files/2015/03/Win15_F_A18_Exhaust_ Nozzle_Chevrons.pdf

[4] How loud is too loud? (n.d.). Retrieved August 22, 2018, from https://www.osha.gov/SLTC/noisehearingconservation/loud.html

[5] Papamoschou, D., Xiong, J., & Liu, F. (2014). Reduction of Radiation Efficiency in High-Speed Jets. *20th AIAA/CEAS Aeroacoustics Conference*. doi:10.2514/6.2014-2619

[6] Ecker, T., Brooks, D. R., Lowe, K. T., & Ng, W. F. (2014). Spectral analysis of over-expanded cold jets via 3-component point Doppler velocimetry. *52nd Aerospace Sciences Meeting*. doi:10.2514/6.2014-1103

[7] Ecker, T., Lowe, K. T., Ng, W. F., & Brooks, D. R. (2014). Fourth-order Spectral Statistics in the Developing Shear Layers of Hot Supersonic Jets. *50th AIAA/ASME/SAE/ASEE Joint Propulsion Conference*. doi:10.2514/6.2014-3742

[8] Ecker, T., Lowe, K. T., & Ng, W. F. (2015). Eddy Convection in Developing Heated Supersonic Jets. *AIAA Journal,53*(11), 3305-3315. doi:10.2514/1.j053946

[9] Ecker, T., Lowe, K. T., & Ng, W. F. (2016). On the Distribution and Scaling of Convective Wavespeeds in the Shear Layers of Heated Supersonic Jets. *Flow, Turbulence and Combustion,98*(2), 355-366. doi:10.1007/s10494-016-9752-3

[10] Mayo, D., Jr., Daniel, K., Lowe, K. T., & Ng, W. F. (n.d.). Experimental Investigation of a Heated Supersonic Jet with Total Temperature Non-Uniformity. Retrieved from https://arc.aiaa.org/doi/pdf/10.2514/6.2017-3521

[11] Mayo, D., Jr., Daniel, K., Lowe, K. T., & Ng, W. F. (n.d.). The Flow and Turbulence Characteristics of a Heated Supersonic Jet with an Offset Total Temperature Non-Uniformity. Retrieved from https://arc.aiaa.org/doi/pdf/10.2514/6.2018-3144

[12] Lighthill, M. J. (1952). On Sound Generated Aerodynamically. I. General Theory. *Proceedings of the Royal Society A: Mathematical, Physical and Engineering Sciences,211*(1107), 564-587. doi:10.1098/rspa.1952.0060

[13] J. E. Ffowcs-Williams, "The Noise from Turbulence Convected at High Speed," *Philos. Trans. R. Soc. London*, vol. 255, no. 1061, pp. 469–503, 1963.

[14] Ffowcs-Williams, J. E. and Maidanik, G. "The Mach wave field radiated by supersonic turbulent shear flows," *J. Fluid Mech.*, vol. 21, no. 4, pp. 641–657, 1965.

[15] M. E. Goldstein and W. L. Howes, "New aspects of subsonic aerodynamic noise theory,"

NASA Tech. Note, no. NASA TN D-7158, pp. 1–41, 1973.
[16] Ribner, H. S. (1969). Quadrupole correlations governing the pattern of jet noise. *Journal of Fluid Mechanics,38*(01), 1. doi:10.1017/s0022112069000012
[17] Murray, N. E., & Lyons, G. W. (2016). On the convection velocity of source events related to supersonic jet crackle. *Journal of Fluid Mechanics,793*, 477-503. doi:10.1017/jfm.2016.127
[18] McIntyre, S., & Settles, G. (1991). Optical experiments on axisymmetric compressible turbulent mixing layers. *29th Aerospace Sciences Meeting*. doi:10.2514/6.1991-623
[19] McIntyre SS (1994) Optical experiments and instrument develop- ment for compressible turbulent mixing layers. PhD thesis, The Pennsylvania State University
[20] Alvi, F., Settles, G., & Weinstein, L. (1993). A sharp-focusing schlieren optical deflectometer. *31st Aerospace Sciences Meeting*. doi:10.2514/6.1993-629
[21] Garg, S., & Settles, G. S. (1998). Measurements of a supersonic turbulent boundary layer by focusing schlieren deflectometry. *Experiments in Fluids,25*(3), 254-264. doi:10.1007/s003480050228
[22] Doty, M. J., & Mclaughlin, D. K. (2005). Space-time correlation measurements of high-speed axisymmetric jets using optical deflectometry. *Experiments in Fluids,38*(4), 415-425. doi:10.1007/s00348-004-0920-1
[23] Petitjean, B., Viswanathan, K., Mclaughlin, D., & Morris, P. (2007). Space-Time Correlation Measurements in Subsonic and Supersonic Jets Using Optical Deflectometry. *13th AIAA/CEAS Aeroacoustics Conference (28th AIAA Aeroacoustics Conference)*. doi:10.2514/6.2007-3613
[24] Papamoschou, D., Morris, P. J., & Mclaughlin, D. K. (2010). Beamformed Flow-Acoustic Correlations in a Supersonic Jet. *AIAA Journal,48*(10), 2445-2453. doi:10.2514/1.j050325
[25] Veltin, J., Day, B. J., & Mclaughlin, D. K. (2011). Correlation of Flowfield and Acoustic field Measurements in High-Speed Jets. *AIAA Journal,49*(1), 150-163. doi:10.2514/1.j050583
[26] Du, Y., & Morris, P. J. (2015). The separation of radiating and non-radiating near-field pressure fluctuations in supersonic jets. *Journal of Sound and Vibration,355*, 172-187. doi:10.1016/j.jsv.2015.06.020
[27] Kerhervé, F., Jordan, P., Gervais, Y., Valière, J., & Braud, P. (2004). Two-point laser Doppler velocimetry measurements in a Mach 1.2 cold supersonic jet for statistical aeroacoustic source model. *Experiments in Fluids,37*(3), 419-437. doi:10.1007/s00348-004-0815-1
[28] Mayo WT Jr, Shay MT, Titter S (1974) Digital estimation of turbulent power spectra from burst counter LDV data. In: Proceedings of 2nd International Workshop on Laser Velocimmetry, Purdue University, pp 16–26
[29] van Maanen HRE, Nobach H, Benedict LH (1999) Improved estimator for the slotted autocorrelation function of randomly sampled LDA data. Meas Sci Tech 10:L4–7

[30] Wernet, M. P. (2007). Temporally resolved PIV for space–time correlations in both cold and hot jet flows. *Measurement Science and Technology,18*(7), 2283-2283. doi:10.1088/0957-0233/18/7/c01

[31] Bridges, J. E., & Wernet, M. P. (2017). Measurements of Turbulent Convection Speeds in Multistream Jets Using Time-Resolved PIV. *23rd AIAA/CEAS Aeroacoustics Conference*. doi:10.2514/6.2017-4041

[32] Lowe, T., Ng, W., & Ecker, T. (2012). Early Development of Time-Resolved Volumetric Doppler Velocimetry for New Insights in Hot Supersonic Jet Noise. *18th AIAA/CEAS Aeroacoustics Conference (33rd AIAA Aeroacoustics Conference)*. doi:10.2514/6.2012-2273

[33] Ecker, T., Brooks, D. R., Lowe, K. T., & Ng, W. F. (2014). Development and application of a point Doppler velocimeter featuring two-beam multiplexing for time-resolved measurements of high-speed flow. *Experiments in Fluids,55*(9). doi:10.1007/s00348-014-1819-0

[34] Hileman, J. I., & Samimy, M. (2006). Mach Number Effects on Jet Noise Sources and Radiation to Shallow Angles. *AIAA Journal,44*(8), 1915-1918. doi:10.2514/1.19959

[35] Komine, H. (1990). *U.S. Patent No. 4919536*. Washington, DC: U.S. Patent and Trademark Office.

[36] Komine, H., Brosnan, S., Litton, A., & Stappaerts, E. (1991). Real-time, Doppler global velocimetry. *29th Aerospace Sciences Meeting*. doi:10.2514/6.1991-337

[37] Meyers JF, Komine H (1991) Doppler global velocimetry: a new way to look at velocity. Laser Anemometry 1:289–296

[38] Ecker, T., Lowe, K. T., & Ng, W. F. (2014). A rapid response 64-channel photomultiplier tube camera for high-speed flow velocimetry. *Measurement Science and Technology,26*(2), 027001. doi:10.1088/0957-0233/26/2/027001

[39] Powers, R., & Mclaughlin, D. (2012). Acoustics Measurements of Scale Models of Military Style Supersonic Beveled Nozzle Jets with Interior Corrugations. *18th AIAA/CEAS Aeroacoustics Conference (33rd AIAA Aeroacoustics Conference)*. doi:10.2514/6.2012-2116

[40] Sean Shea, Kevin T. Lowe, and Wing F. Ng. "Eddy Convection in Cold and Heated Supersonic Jets", 23rd AIAA/CEAS Aeroacoustics Conference, AIAA AVIATION Forum, (AIAA 2017-4044) https://doi.org/10.2514/6.2017-4044

[41] Morris, P.J. and Zaman, K.B.M.Q., "Velocity Measurements in Jets with Application to Noise Source Modeling," AIAA 2009-17 47th AIAA Aerospace Sciences Meeting, 05 January 2009

[42] Witze, P. O. (n.d.). Centerline Velocity Decay of Compressible Free Jets. Retrieved from https://arc.aiaa.org/doi/abs/10.2514/3.49262

[43] Sinha, Aniruddha, et al. "Toward Active Control of Noise from Hot Supersonic Jets." 19th AIAA/CEAS Aeroacoustics Conference, 2013, doi:10.2514/6.2013-2234.

[44] Kleinstein, G. (1964). Mixing in turbulent axially symmetric free jets. *Journal of Spacecraft and Rockets,1*(4), 403-408. doi:10.2514/3.27669

Appendix

A.1 PMT Sensor Calibration Results

Summary of Contents

Tests were conducted to determine the ability of a mask to assist with data collection using the DGV cameras. While varying the light intensity and optical arrangement of ND filters in front of the PMTs, the response was recorded, averaged, and baseline subtracted to determine the change in counts recorded by each individual channel. The linearity of the responses was qualitatively observed and are presented for several cases below. In addition, heat-maps are presented to demonstrate the effect of hardware on the recorded signals. Finally, a single case of not using a mask is presented for comparison.

The goals of these tests were to see the maximum allowable counts that a PMT could read at ~750V before saturation were to occur while using a mask over the PMT. This was done by varying the strength of Neutral density filters used to cut the light reaching the PMTs. The following document shows the transition period where the response from the PMTs became oversaturated. Due to a limited supply of ND filters, finer detail in the PMT responses than those presented below is not possible.

Figures A.1a and A.1b are from an experiment where only 0.00882% of the light was allowed to reach the sensor. It is apparent that the response for each PMT is linear but there is one pixel on Cam 3 (Fig A.1b.) that is reading higher than the other pixels. This is a behavior that would be expected if only that pixel were receiving light. Typically the pixels are grouped together as shown in Fig A.1a.

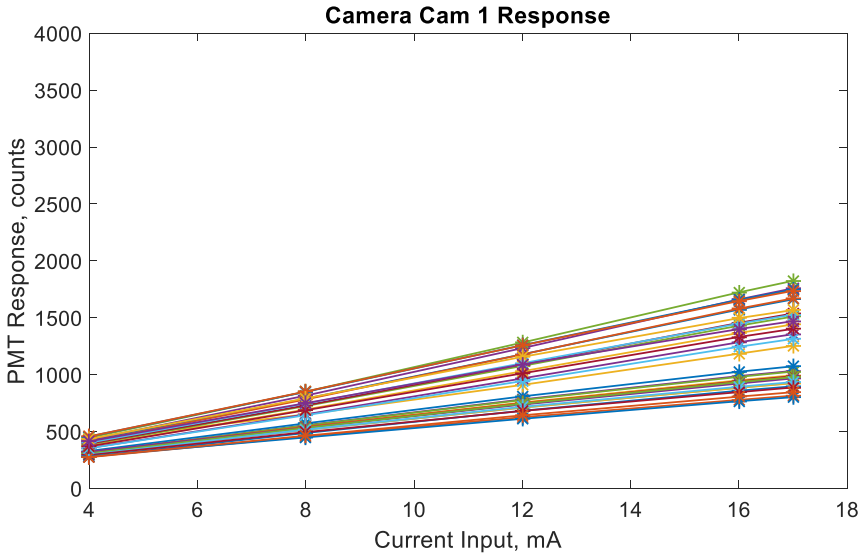

Figure A.1a Cam 1 response for light transmission of 0.00882%

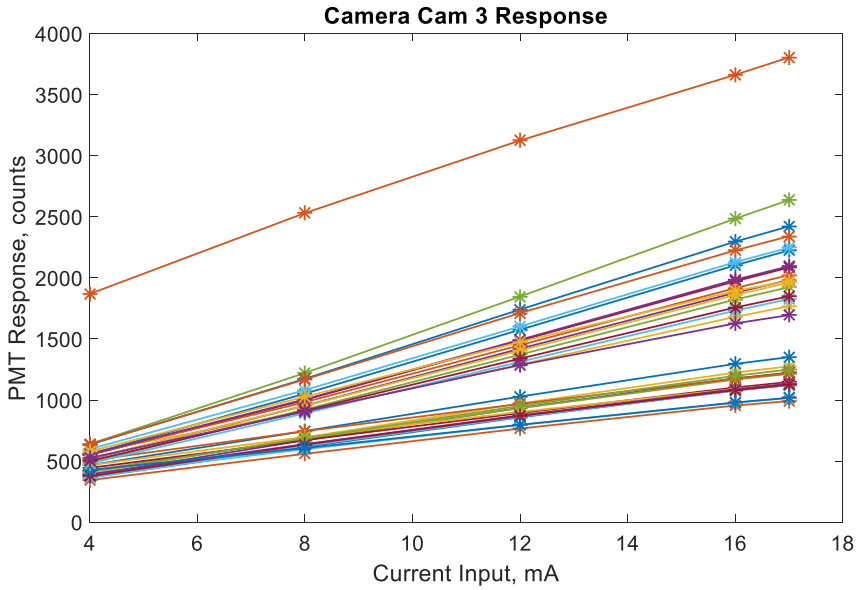

Figure A.1b Cam 3 response for light transmission of 0.00882%

Figures A.2a and A.2b show a very interesting result for when 0.0114% of the light was transmitted. In figure A.2a, the response of the pixels still appears rather linear, however in A.2b, we start to see some deviation from linearity, especially in the channel that was already higher than the others. Interestingly, the deviation starts in every pixel at the same location as where the odd channel severely the nonlinearity.

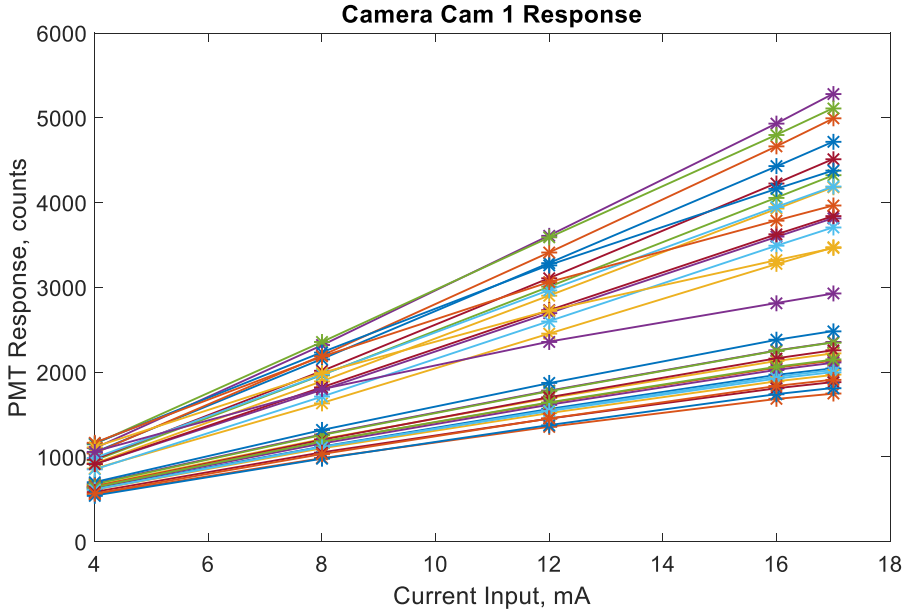

Figure A.2a Cam 1 response for light transmission of 0.0114%

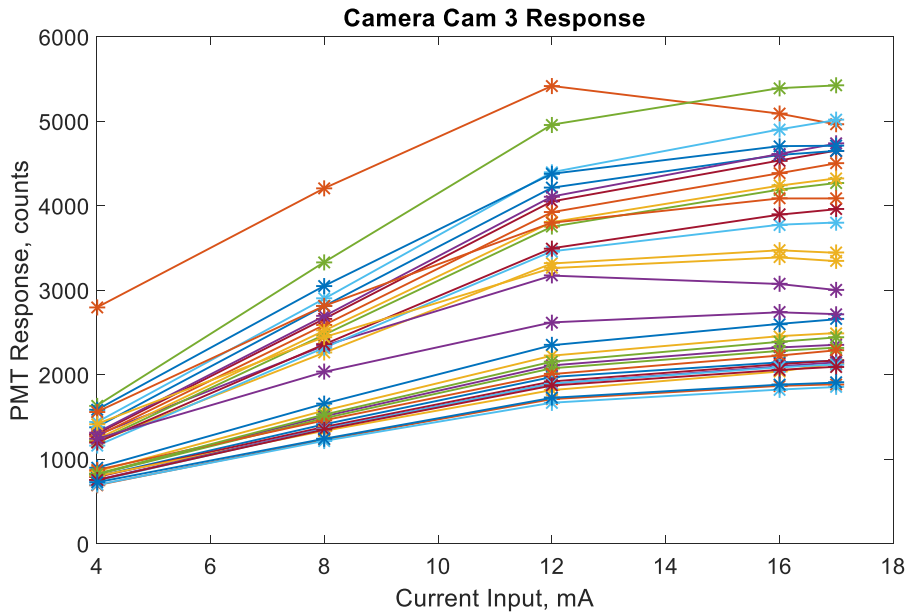

Figure A.2b Cam 3 response for light transmission of 0.0114%

Figures A.3a and A.3b show the results for the 0.0365% transmission case. In both cases, the signals are beginning to go nonlinear. In Figure A.3b it still appears that the odd channel determines when the rest of the pixels become nonlinear.

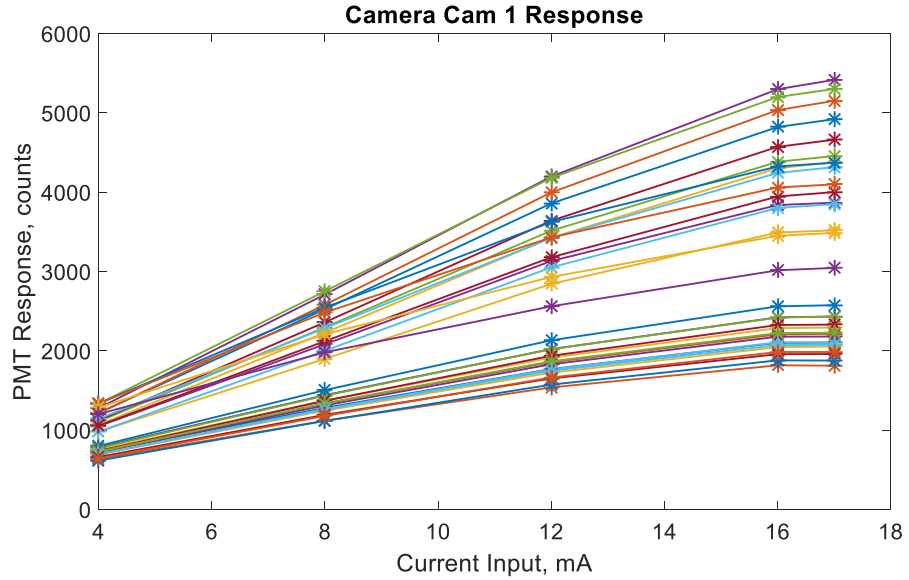

Figure A.3a Cam 1 response for light transmission of 0.0365%

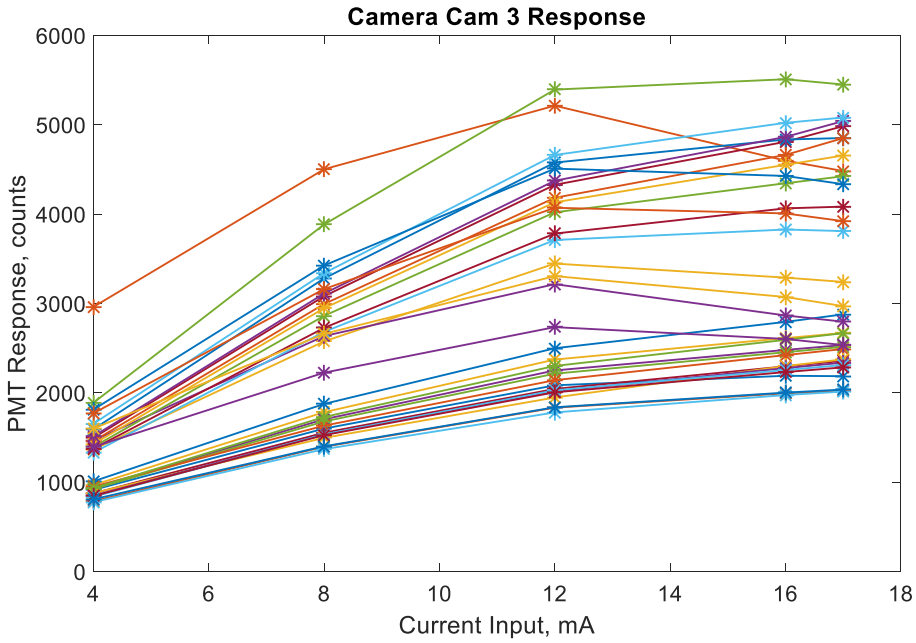

Figure A.3b Cam 3 response for light transmission of 0.0365%

Figures A.4a and A.4b are the PMT response from a different day but with more data points. The goal here was to get a better idea of when the PMT response would become nonlinear while using a mask. This was a repeat of the 0.0114% case since that was the first case where nonlinearity appeared in the results. It should be noted that the "odd" channel becomes nonlinear at approximately 5200 counts (Fig. 4b). It should also be noted that in this test, the x-coordinate at which the response becomes nonlinear is the same as the previous test. Interestingly, in this test, the response of the PMT associated with Cam 1 (Fig. A.4a) also started to become nonlinear, something that was not observed in Figure A.2a. In addition to this, it is also becoming nonlinear below 5000 counts, again this was not shown in earlier tests.

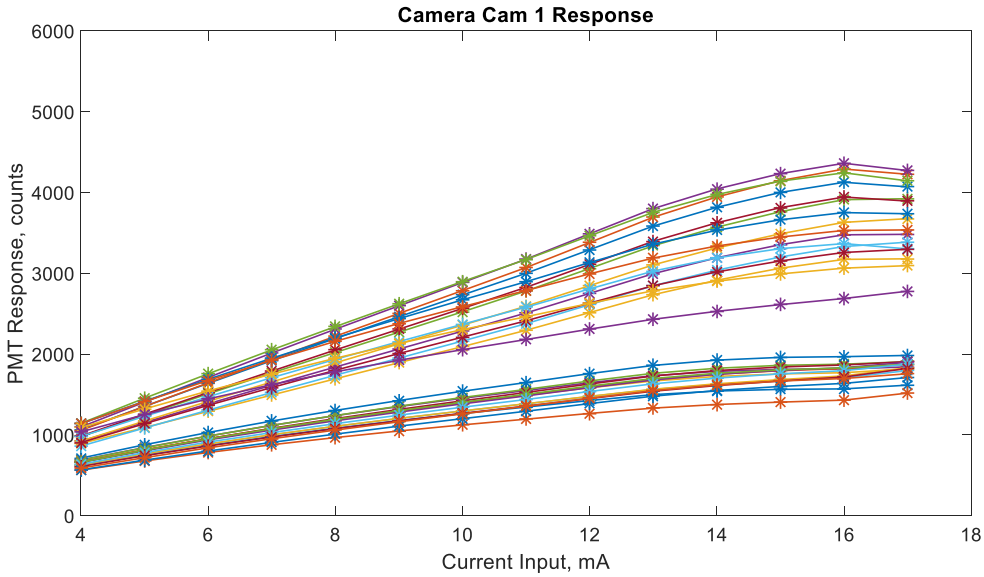

Figure A.4a Cam 1 response for light transmission of 0.0114%

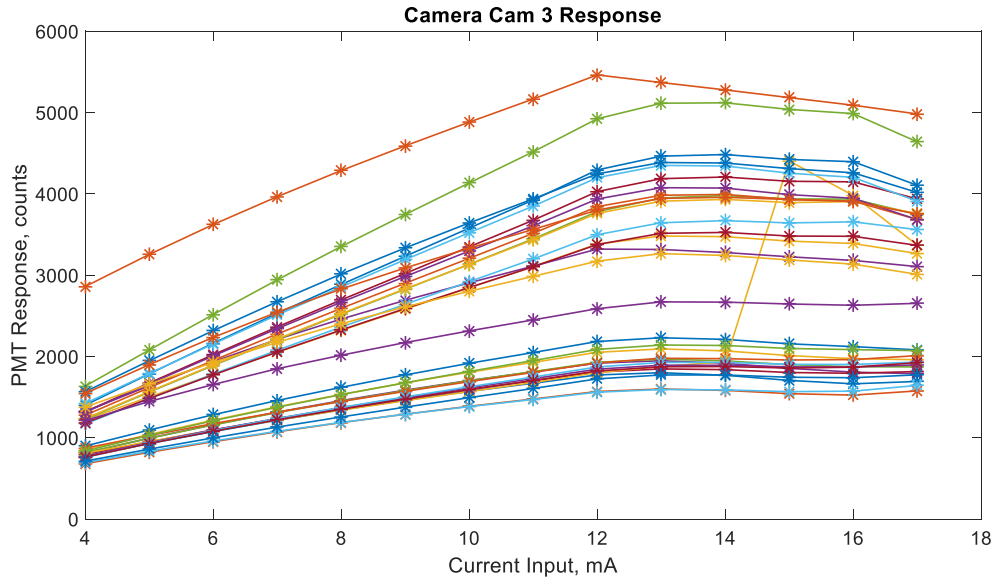

Figure A.4b Cam 3 response for light transmission of 0.0114%

No Mask Case

Figures A.5a and A.5b show the PMT response without the use of a mask and with a transmission of 0.00261%. The most significant thing to note here is that the PMT response remained linear even though the "odd" channel is registering nearly 6800 counts, well over what was seen while using the mask.

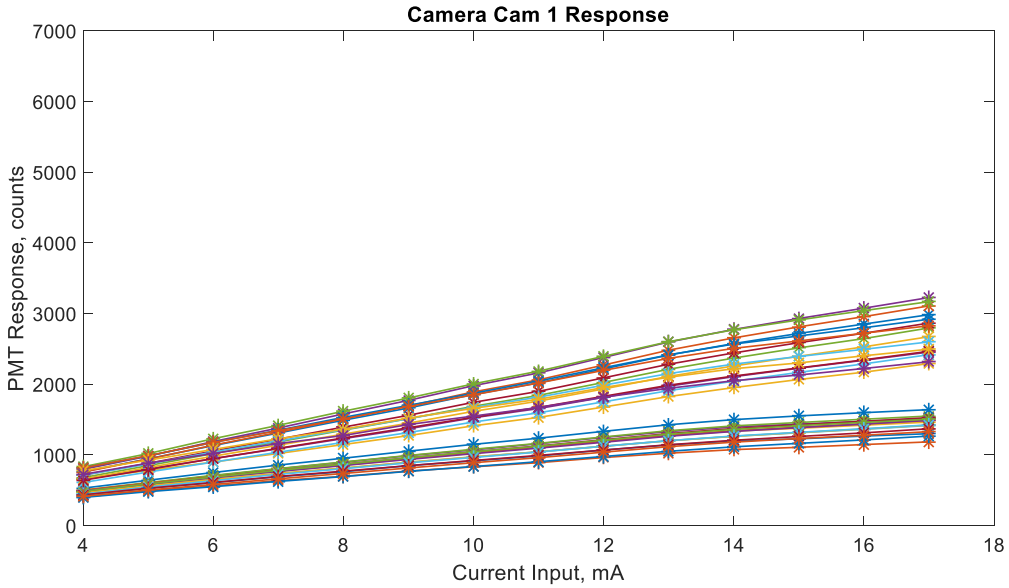

Figure A.5a Cam 1 response for light transmission of 0.00261% and no mask

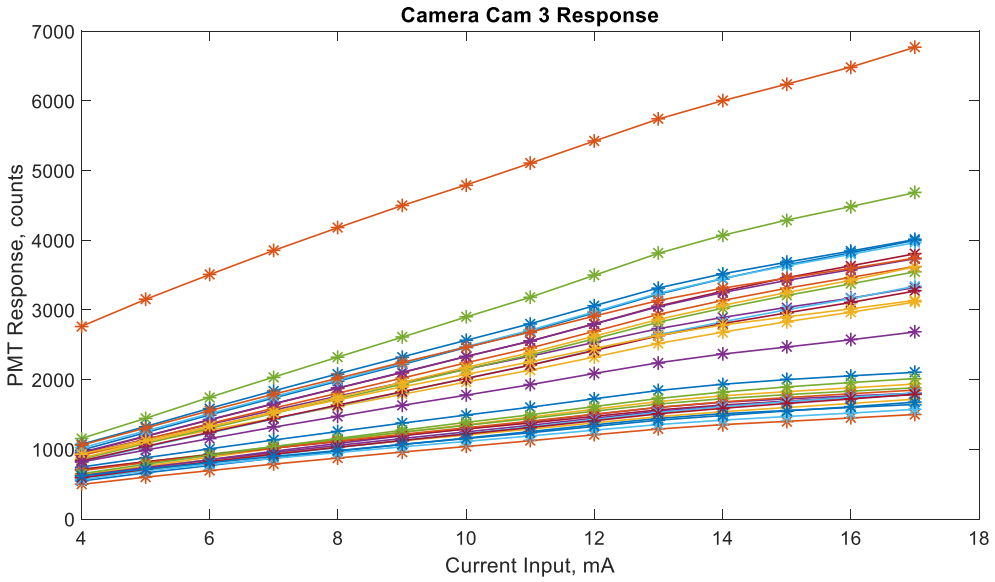

Figure A.5b Cam 3 response for light transmission of 0.00261% and no mask

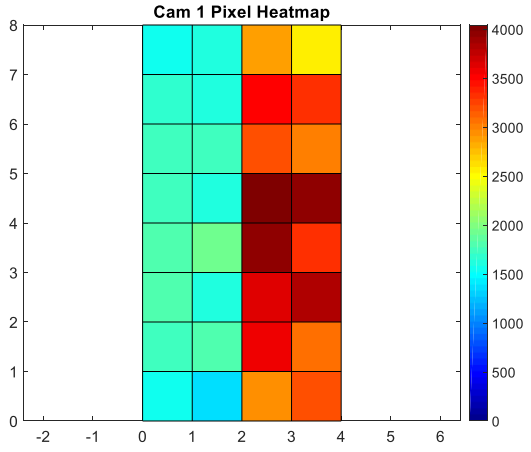

Figure A.6a – Cam 1, 0.0114% case heat-map

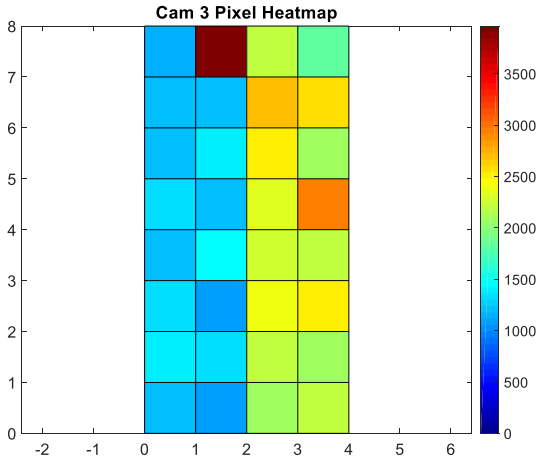

Figure A.6b – Cam 3, 0.0114% case heat-map

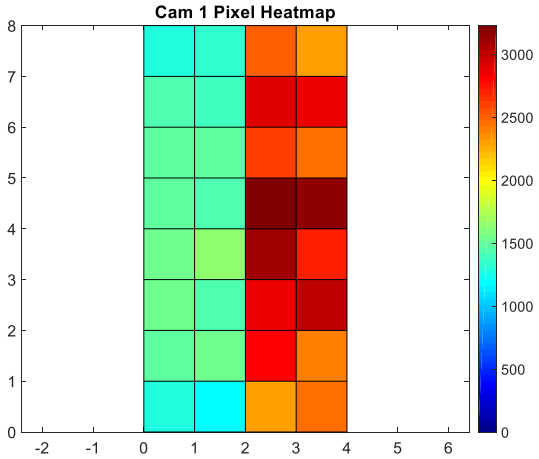

Figure A.6c – Cam 1, 0.00261% case heat-map

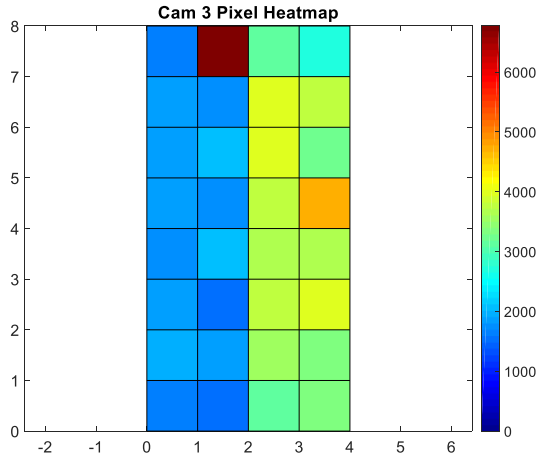

Figure A.6d – Cam 1, 0.00261% case heat-map

Figures A.6a-A.6d show a sample mapping of the average counts recorded by each pixel as mapped onto the PMT sensor. Figs. A.6a and A.6b are a mapping when a mask covered the PMTs and Figs. A.6c and A.6d are for the case without a mask. As demonstrated by figures, the overall color pattern does not change, only the intensity recorded by the PMTs. What is interesting, is that in each case, it is seen that there are two bands of coloring, which can be explained with the hardware arrangement within a camera. Every two columns is connected to a different signal amplifier board which could account for this difference. What is also interesting is that the "hotter" colors occur on the same side of the PMT. The only explanation for this is that it may have something to do with there the power goes into the amplifier boards. However, it should be noted that the amplifier card which receives the main power line corresponds to the pixels with "cooler" colors.

Final Thoughts

- With a mask, the intensity of the light received by each PMT sensor may be greater, however the response becomes nonlinear near 5000 counts.
- Without a mask, the incident light intensity needs to be reduced. In addition, the response was observed to be linear for the inputs tested and resulted in a response greater than 5000 counts.
- No mask is more than likely a better option, however ND filters may be needed.
- If one pixel starts to behave in a nonlinear fashion, it adversely affects the other pixels on the same PMT.
- The amplifier boards appear to affect the response and explain the groupings in the responses of the PMTs.
- The heat-maps clearly show that there appears to be a single defective pixel on this pair of PMT sensors.
- There is no difference in the pattern of the heat-maps between having a mask and not.

A.2 Convection Velocity from Correlation Troughs

This Appendix summarizes efforts to use portions of the correlation function, other than the location of the peak correlation value, to determine speeds of other flow features. The working hypothesis was that if the velocity from the first trough of the correlation function was large, then the local eddies would be larger than in neighboring areas. This is because larger, more coherent structures are present near the core of the jet. The sample data chosen for this analysis is from the Mach 1.65 *TTR* = 1 jet discussed in Section 4 of the current work at an axial station of 8*D* to ensure that the data included part of the potential core. The trough of the correlation function is depicted in Figure A.2.1.

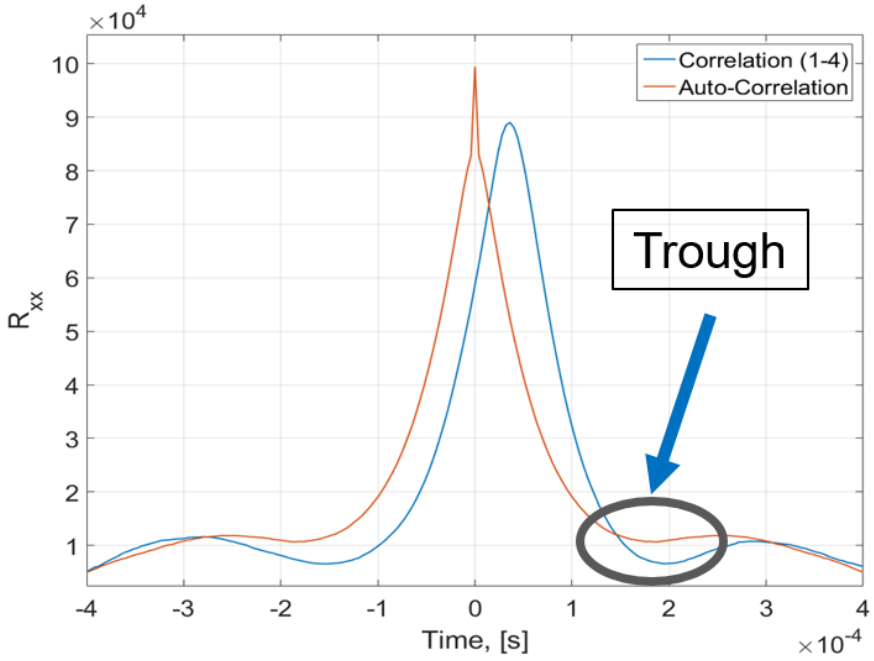

Figure A.2.1 Depiction of positive trough in correlation function.

In order to compute the trough velocity U_{trough} defined in Equation (A.1), a local minimum was identified on the auto-correlation and the correlation between the furthest spaced pixels of the PMT sensor. The identification of the local minima of the correlation functions can be seen in Figure A.2.2. Note that multiple minima are found, but only minimum corresponding with the trough are used in the calculation of the trough velocity. A fit is applied between the minimum

found and the adjacent points to determine an interpolated, true minimum. These true minimums are displayed with vertical light blue and green lines.

$$U_{trough} = \frac{\Delta x}{\tau_1 - \tau_2}$$

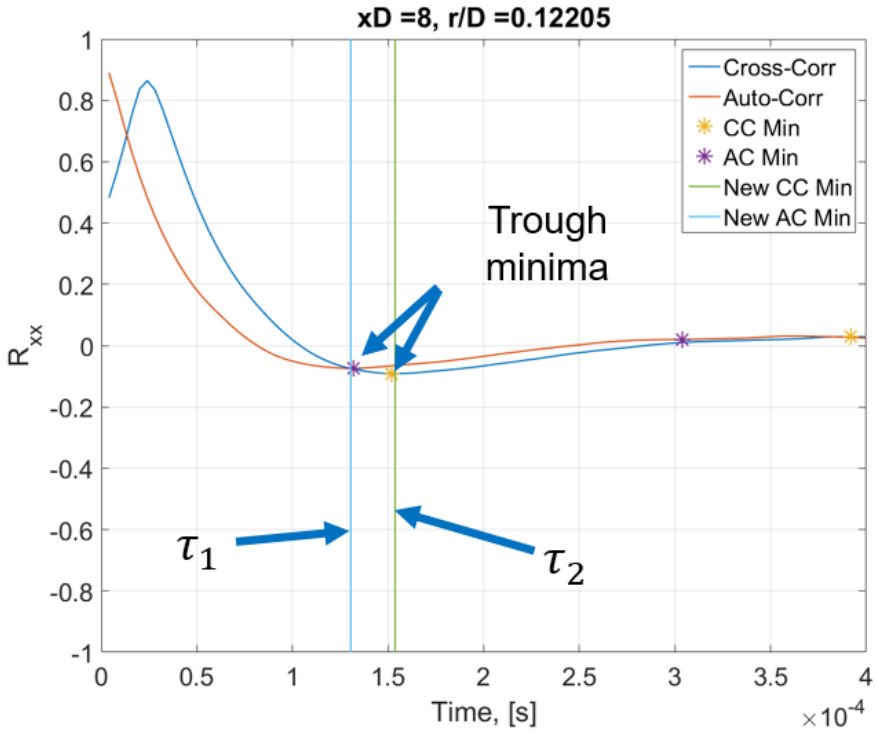

Figure A.2.2 Finding the local minimum of correlations curves at r/D = 0.12.

In the above equation, the value of τ_1 and τ_2 are the values of the true minimum and Δx is the distance traversed by particles within the flow.

During this analysis, it was noted that as correlations moved radially out into the shear layer, it became more difficult to find a trough minimum since the troughs became more shallow and in some cases there was no minima in the desired time range. It was also noted that the trough moves outward away from zero time lags when the location of the correlation moves away from the centerline. These features are displayed in Figure A.2.3.

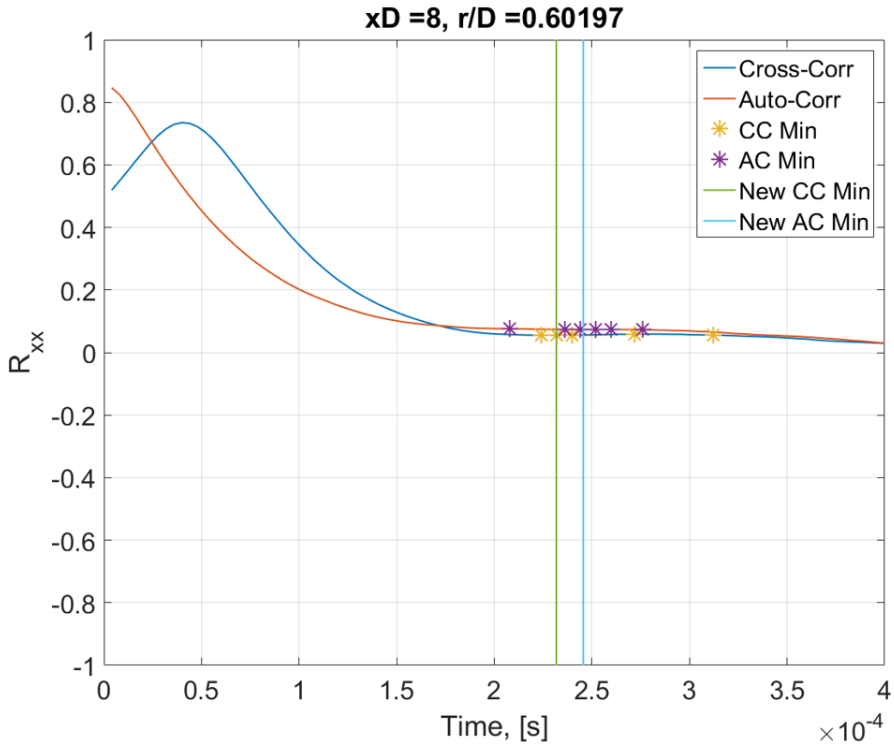

Figure A.2.3 Local minimum of correlations curves at r/D = 0.60.

To overcome the issue of the auto-correlation curve not having a minimum, the correlation between the closest spaced pixels (pixel 1 and pixel 2) was used since there should be a high correlation between these pixels similar to a correlation between pixel 1 and itself. This, however only had a very small impact at being more able to find a local minimum.

Figures A.2.4 and A.2.5 display the computed convection velocities and the time differences τ_1-τ_2, respectively. In these figures the line labeled "Real" corresponds to the actual measured value of the conveciton velocity. The other lines correspond to the trough velocity computed while using the auto-correlation for τ_1 ("Auto-4" in the figure) or using the correlation between pixels 1 and 2 for τ_1 ("2-4" in the figure). In both cases, the correlation used for τ_2 remained the same; the correlation between the furthest spaced pixels as is typical in computing convection velocity.

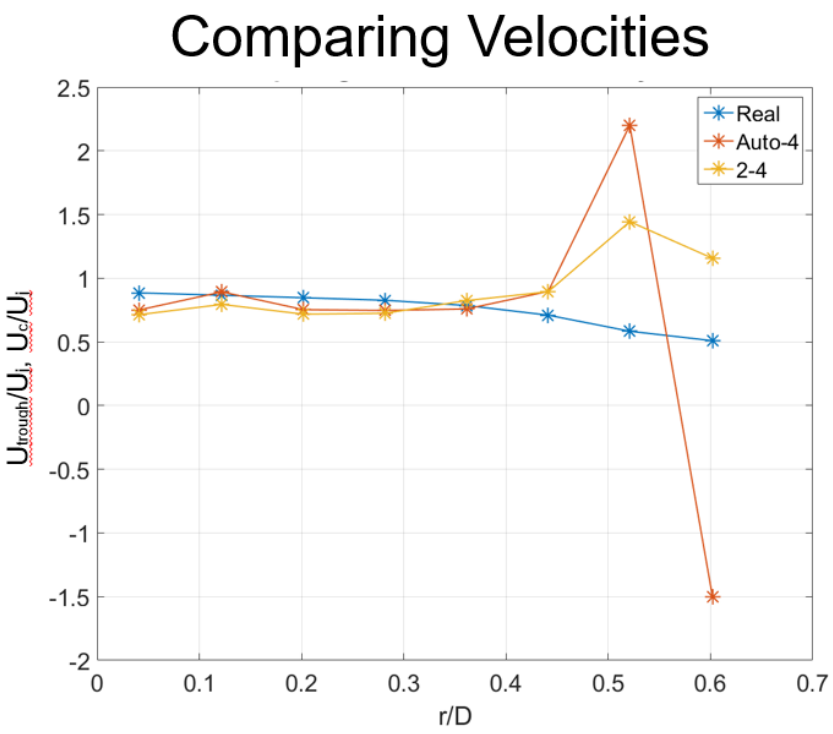

Figure A.2.4 Trough velocity results.

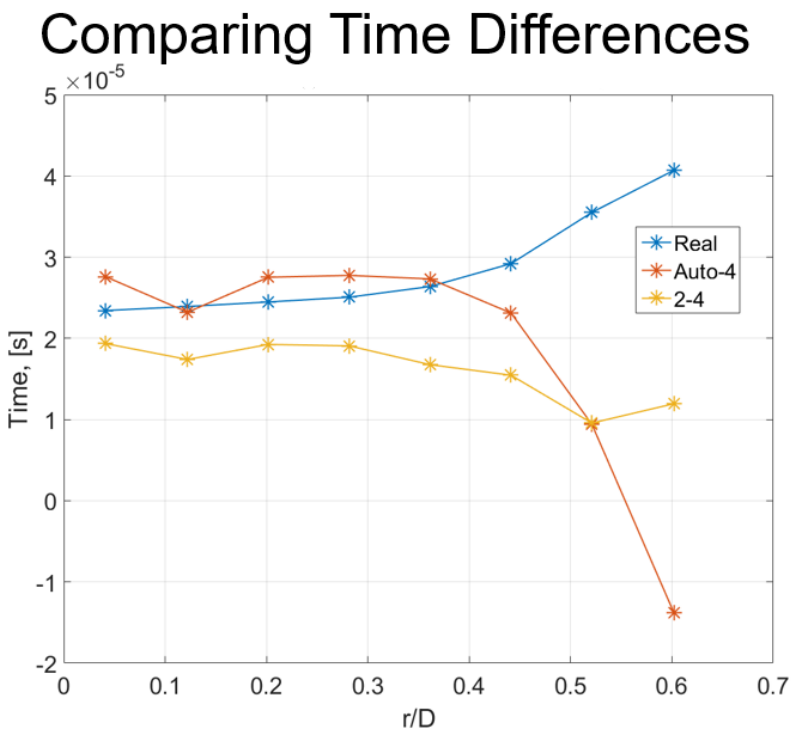

Figure A.2.5 Time difference between methods.

From the figure, it is clear that in general, as the convection velocity decreases, the trough velocity increases. This is an unexpected result as it was thought that the larger and faster moving structures would be closer to the centerline of the jet. Another item of note is that there is a large negative trough velocity, due to the presence of a large negative time difference. Upon further inspection, this was due to the location of the trough of the auto-correlation occurred later in time than the correlation used for τ_2.

One possible source for the unexpected result is displayed in Figure A.2.6. As displayed in this plot of the power spectra for a pixel used in this analysis, it was noted and a 1068 Hz and 2899 Hz tone are present. Minimizing these tones using a filter may improve the results of the above analysis, but this may also filter out desired data.

A few unanswered questions remain. First, there appears to be a trend in the trough velocities and their respective time differences. If the original hypothesis is incorrect, which it appears to be, what is actually being measured? Second, would filtering the data be beneficial? Due to time restrictions, this was not completed. Finally, what data would be useful, in the future, in getting more information out of this data? In the opinion of the author, more TR-DGV measurements could be done with a higher magnification in the investigation window. Additionally, upgrading the system to utilize all available pixels would help with getting more points within the flow and be able to get a larger distance over which to compute the convection and trough velocities. PIV and LDV investigations may also be of use in expanding the results of this analysis.

Overall, this analysis demonstrated that the trough of the correlation output has potential to yield some information about the flow, but it is still unclear exactly what is being measured.

A.3 Alternative Peak Correlation Velocities

Preliminary work was done on looking at convection velocities using correlations between different pixels. It was believed that by looking at the different correlations, different velocities would be indicative of the different speeds of the dominant structures over the correlation distance. Since the PMT sensors have four pixels in a row, it would be possible to compute three different convection velocities. Unfortunately after computation of the three resulting convection velocities, it was determined that they were too close to each other and each resided within the estimated error of each other. This result is displayed in Figure A.3.1 below.

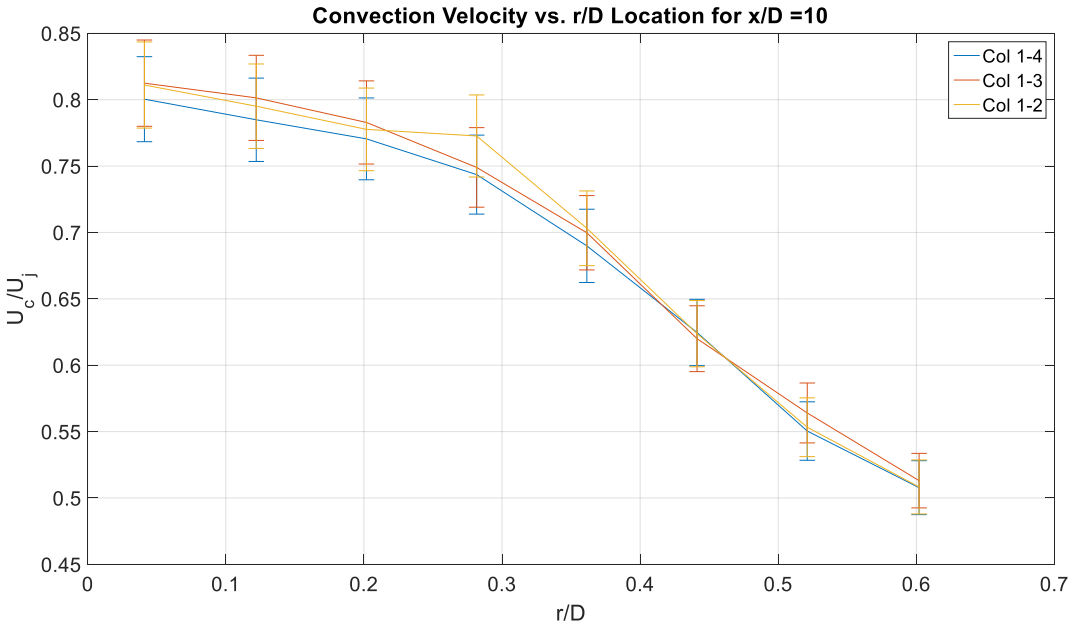

Figure A.3.1 Radial convection profiles of the three convective speed at x/D = 10.

It would appear that the main limiting factor with this technique is the absolute error in TR-DGV. If there was a way to reduce the error by averaging records without hindering the temporal resolution, this may help.